

Hot ammonia around young O-type stars

III. High-mass star formation and hot core activity in W51 Main[★]

C. Goddi^{1,2}, A. Ginsburg³, and Q. Zhang⁴

¹ Department of Astrophysics/IMAPP, Radboud University Nijmegen, PO Box 9010, 6500 GL Nijmegen, The Netherlands
e-mail: c.goddi@astro.ru.nl

² ALLEGRO/Leiden Observatory, Leiden University, PO Box 9513, 2300 RA Leiden, The Netherlands

³ ESO, Karl-Schwarzschild-Strasse 2, 85748 Garching bei München, Germany

⁴ Harvard-Smithsonian Center for Astrophysics, 60 Garden Street, Cambridge, MA 02138, UK

Received 27 November 2015 / Accepted 25 January 2016

ABSTRACT

Context. This paper is the third in a series of NH₃ multilevel imaging studies in well-known, high-mass star-forming regions. The main goal is to characterize kinematics and physical conditions of (hot and dense) circumstellar molecular gas around O-type young stars.

Aims. We want to map at subarcsecond resolution highly excited inversion lines of NH₃ in the high-mass star-forming region W51 Main (distance = 5.4 kpc), which is an ideal target to constrain theoretical models of high-mass star formation.

Methods. Using the Karl Jansky Very Large Array (JVLA), we mapped the hot and dense molecular gas in W51 Main with $\sim 0''.2$ – $0''.3$ angular resolution in five metastable ($J = K$) inversion transitions of ammonia (NH₃): (J, K) = (6, 6), (7, 7), (9, 9), (10, 10), and (13, 13). These lines arise from energy levels between ~ 400 K and ~ 1700 K above the ground state. We also made maps of the (free-free) continuum emission at frequencies between 25 and 36 GHz.

Results. We have identified and characterized two main centers of high-mass star formation in W51 Main, which excite hot cores and host one or multiple high-mass young stellar objects (YSOs) at their centers: the W51e2 complex and the W51e8 core ($\sim 6''$ southward of W51e2). The former breaks down into three further subcores: W51e2-W, which surrounds the well-known hypercompact (HC) HII region, where hot NH₃ is observed in absorption, and two additional dusty cores, W51e2-E ($\sim 0''.8$ to the East) and W51e2-NW ($\sim 1''$ to the North), where hot NH₃ is observed in emission. The velocity maps toward the HC HII region show a clear velocity gradient along the east-west in all lines. The gradient may indicate rotation, although any Keplerian motion must be on smaller scales (< 1000 AU) as we do not directly observe a Keplerian velocity profile. The absence of outflow and/or maser activity and the low amount of molecular gas available for accretion ($\sim 5 M_{\odot}$, assuming $[\text{NH}_3]/[\text{H}_2] = 10^{-7}$) with respect to the mass of the central YSO estimated from radio luminosity ($> 20 M_{\odot}$), both indicate that the central YSO has already accreted most of its final mass. On the other hand, the nearby W51e2-E, while not showing evidence of rotation, shows signatures of infall in a hot dense core ($T \sim 170$ K, $n_{\text{H}_2} \sim 5 \times 10^7 \text{ cm}^{-3}$), based on asymmetric spectral profiles (skewed toward the blueshifted component) in optically thick emission lines of NH₃. The relatively large amount of hot molecular gas available for accretion ($\sim 20 M_{\odot}$ within about half an arcsecond or 2500 AU), along with strong outflow and maser activity, indicates that the main accretion center in the W51e2 complex is W51e2-E rather than W51e2-W. Finally, W51e2-NW and W51e8, although less dense ($n_{\text{H}_2} \sim 2 \times 10^7 \text{ cm}^{-3}$ and $\sim 3 \times 10^6 \text{ cm}^{-3}$), are also hot cores ($T_{\text{gas}} \sim 140$ and 200 K) and contain a significant amount of molecular gas ($M_{\text{gas}} \sim 30 M_{\odot}$ and $\sim 70 M_{\odot}$, respectively). We speculate that they may host high-mass YSOs either at a previous evolutionary stage or with a mass that is lower than W51e2-E and W51e2-W.

Conclusions. Using high-angular resolution multilevel imaging of highly excited NH₃ metastable lines, we characterized the physical and dynamical properties of four individual high-mass young stars forming in the W51 Main clump.

Key words. accretion, accretion disks – line: profiles – ISM: kinematics and dynamics – ISM: molecules – stars: protostars – HII regions

1. Introduction

W51 (at 5.4 kpc; Xu et al. 2009) is one of the most luminous high-mass star-forming regions (HMSFRs) in the Galaxy with a luminosity of about $\sim 2 \times 10^7 L_{\odot}$ (within a 2 pc radius), implying a total stellar mass of about $7000 M_{\odot}$, corresponding to at least 20 O-type stars (i.e., greater than $20 M_{\odot}$; Ginsburg et al. 2016). These massive stars are associated with three main regions: W51 IRS1, W51 IRS2 ($30''$ northwest or NW of IRS1), and W51 Main ($30''$ southeast or SE of IRS1). While W51 IRS1 is associated with an evolved HII region (size ~ 1 pc) and is deprived of molecular gas or dust, W51 Main and W51 IRS2

are sites of active high-mass star formation (HMSF). This paper is the third in a series of NH₃ multilevel imaging studies in luminous HMSFRs associated with strong hot core activity, presumably hosting O-type stars forming at their centers (for a general description, see Goddi et al. 2015a; hereafter Paper I). A study on W51 IRS2 was reported in the second paper of the series (Goddi et al. 2015b; hereafter Paper II). This paper focuses on W51 Main.

W51 Main is a very active region of HMSF and contains a cluster of ultracompact (UC) and hypercompact (HC) HII regions, labeled e1 to e8 (Gaume et al. 1993; Mehringer 1994; Zhang & Ho 1997). The region shows widespread NH₃ thermal emission (Zhang & Ho 1997) as well as strong maser emission from OH, CH₃OH, H₂O, and NH₃ (Zhang & Ho 1995; Imai et al. 2002; Fish & Reid 2007; Etoaka et al. 2012; Surcis et al. 2012).

[★] The reduced NH₃ data cubes as FITS files are only available at the CDS via anonymous ftp to cdsarc.u-strasbg.fr (130.79.128.5) or via <http://cdsarc.u-strasbg.fr/viz-bin/qcat?J/A+A/589/A44>

W51e2 is the strongest and best-studied HC HII region in the W51 Main cluster, and it is believed to be powered by an O8-type young star (e.g., Shi et al. 2010a). A number of interferometric studies conducted with varying angular resolutions, at centimetre (cm) and (sub)millimetre (mm) bands, identified molecular and ionized gas undergoing infall and rotation toward W51e2. VLA observations of the NH₃ inversion lines (1, 1) and (2, 2) seen in absorption (1′′ beamsize) revealed radial infall on scales larger than 5000 AU toward the W51e2 core (Zhang & Ho 1997). Higher angular resolution observations of the (3, 3) NH₃ absorption line (0′.3 beamsize) showed signatures of rotation within 2000 AU based on a position-velocity (pv) diagram (Zhang & Ho 1997). Zhang et al. (1998) identified a velocity gradient in a CH₃CN transition at 2 mm, deriving a position angle (PA) of $20 \pm 20^\circ$. Keto & Klaassen (2008) imaged the H53 α radio recombination line (RL) with the VLA (0′.45 beamsize) and they claimed rotation in the ionized gas along the axis of a molecular bipolar outflow (oriented NW-SE) imaged with the SMA in the CO (2–1) line (1′′ beamsize), suggesting a simple inflow/outflow picture in a single high-mass young stellar object (YSO). However, higher resolution observations, using the SMA at the wavelengths of 0.85 mm (0′.3 beamsize) and 1.3 mm (0′.7 beamsize), revealed a more complex picture, by resolving W51e2 into three subcores (Shi et al. 2010a): W51e2-W, corresponding to the HC HII region, W51e2-E, located about 1′′ east of the HC HII region and corresponding to the brightest dust continuum source, and W51e2-NW, the weakest continuum component, located about 1′′ NW of the HC HII region. Shi et al. (2010b) imaged the CO (3–2) line (with a 0′.7 beamsize) and established that the driving source of the powerful molecular outflow in this region is the protostellar core W51e2-E, and not the HC HII region W51e2-W, challenging the scenario proposed by Keto & Klaassen (2008). Etoke et al. (2012) used MERLIN to image the Class II 6.7 GHz CH₃OH masers (typical signpost of HMSF), and found that the bulk of maser emission is indeed concentrated toward W51e2-E, and not the HC HII region W51e2-W. This further supports the scenario proposed by Shi et al. (2010a), where the ongoing star formation activity in the region is not concentrated on the HC HII region but toward its companion 1′′ to the east.

While the subarcsecond SMA study was successful in resolving multiple components, a multilevel imaging study of the same molecule at subarcsecond resolution is required to study the kinematics and the physical conditions of hot molecular gas surrounding individual high-mass YSOs, and thus characterize their physical properties. With this in mind, we imaged five NH₃ inversion lines with energy levels high above the ground state (equivalent to 400–1700 K) at an angular resolution of about 0′.2 toward W51 Main.

The current paper is structured as follows. The observational setup and data calibration procedures are described in Sect. 2. Maps and spectral profiles of different maser transitions are presented in Sect. 3. In Sect. 4 we present our analysis of the physical conditions of the molecular gas based on the NH₃ measurements. In Sect. 5, we discuss the star formation activity in W51 Main. Finally, our conclusions are drawn in Sect. 6.

2. Observations and data reduction

Observations of NH₃ toward the W51 complex were conducted using the Karl G. Jansky Very Large Array (JVLA) of the

National Radio Astronomy Observatory (NRAO)¹ in the B configuration. The observing setup and data reduction procedures were already described in detail in Papers I and II; but we summarize them here as well. By using the broadband JVLA K- and Ka-band receivers, we observed a total of five metastable inversion transitions of NH₃: (J, K) = (6, 6), (7, 7), (9, 9), (10, 10), and (13, 13) at the 1 cm band with frequencies ranging from ≈ 25 GHz for the (6, 6) line to ≈ 33 GHz for the (13, 13) line. Transitions were observed in pairs of independently tunable basebands during 6h tracks (two targets per track: W51 – this paper; NGC 7538 IRS1 – Paper I) on three different dates in 2012: the (6, 6) and (7, 7) lines on May 31 at K-band, the (9, 9) and (13, 13) lines on June 21, and the (10, 10) transition on August 7, both at Ka-band. Each baseband had eight sub-bands with a 4 MHz bandwidth (≈ 40 km s⁻¹ at 30 GHz), providing a total coverage of 32 MHz (≈ 320 km s⁻¹ at 30 GHz). Each sub-band consisted of 128 channels with a separation of 31.25 kHz (≈ 0.3 km s⁻¹ at 30 GHz). The typical on-source integration time was about 80 min. Each transition was observed with fast switching, where 80s scans on target were alternated with 40s scans on the nearby (1.2° on the sky) QSO J1924+1540 (measured flux density 0.6–0.7 Jy, depending on frequency). We derived absolute flux calibration from observations of 3C 48 ($S_\nu = 0.5$ –0.7 Jy, depending on frequency), and bandpass calibration from observations of 3C 84 ($S_\nu = 27$ –29 Jy, depending on frequency).

The data were edited, calibrated, and imaged in a standard fashion using the Common Astronomy Software Applications (CASA) package. We fitted and subtracted continuum emission from the spectral line data in the uv plane using CASA task UVCONTSUB, combining the continuum (line-free) signal from all eight sub-bands around the NH₃ lines. Before imaging, we performed self-calibration on the strong (6, 6) NH₃ maser detected in W51-north (velocity of 47.6 km s⁻¹, and peak flux density ~ 5 Jy; see Paper II). We then applied the self-calibration solutions from the reference channel with the maser to the dataset containing the lines (6, 6) and (7, 7)². Since the (9, 9) maser line was much weaker than the (6, 6) line (peak flux density ~ 0.4 Jy), we did not perform self-calibration on the dataset containing the (9, 9) and (13, 13) lines (nor the 10, 10 transition). Using the CASA task CLEAN, we imaged the W51 Main region with a cell size of 0′.04, covering a 20′′ field around the position $\alpha(J2000) = 19^{\text{h}}23^{\text{m}}43^{\text{s}}.90$, $\delta(J2000) = +14^\circ30'34''.6$. We adopted Briggs weighting with a ROBUST parameter set to 0.5 and smoothed the velocity resolution to 0.4 km s⁻¹, for all transitions. The resulting synthesized clean beam FWHM were 0′.19–0′.26 (depending on frequency) and the typical root mean square (rms) noise level per channel was ≈ 1.5 mJy beam⁻¹. This is the case except for the dataset containing the (10, 10) doublet, which was noisier because of bad atmospheric conditions and other issues. Since the observations were conducted pointing the telescopes at W51-IRS1 (with a sky position of $\alpha(J2000) = 19^{\text{h}}23^{\text{m}}42^{\text{s}}.00$, $\delta(J2000) = +14^\circ30'50''.0$), to include both W51-IRS2 and W51 Main in the JVLA antennae's primary beam, we applied primary beam corrections during cleaning (on

¹ NRAO is a facility of the National Science Foundation operated under cooperative agreement by Associated Universities, Inc.

² While the self-calibration solutions had a significant effect on the image quality of the maser line, improving its dynamic range by a factor of 4, they had a more limited effect on the images of the continuum and the NH₃ thermal line emission (the latter occurs at a different velocity with respect to the maser, ~ 57 km s⁻¹ vs. ~ 47 km s⁻¹, respectively; see Paper II). The quality of the final maps obtained applying the self-calibration solutions was nevertheless also better in the case of thermal emission.

Table 1. Parameters of JVLA observations toward W51.

Transition ^a (<i>J</i> , <i>K</i>)	ν_{rest} (MHz)	E_u/k^b (K)	Date (yyyy-mm-dd)	JVLA receiver	Beamwidth ^c $\theta_M(\prime) \times \theta_m(\prime)$; PA(°)	RMS ^d (mJy/beam)
NH ₃						
(6, 6)	25 055.96	408	2012-May-31	K	0.29 × 0.23; -17	1.5
(7, 7)	25 715.44	539	2012-May-31	K	0.28 × 0.23; -2	1.6
(9, 9)	27 477.94	853	2012-Jun-21	Ka	0.24 × 0.22; +53	1.3
(10, 10)	28 604.75	1035	2012-Aug-07	Ka	0.23 × 0.21; +61	2.9
(13, 13)	33 156.84	1691	2012-Jun-21	Ka	0.20 × 0.18; +52	1.9
Other molecular transitions						
CH ₃ OH ^e	27 472.53	234	2012-Jun-21	Ka	0.24 × 0.22; +53	1.3
CH ₃ CN ^f	36 793.71	10	2012-Aug-07	Ka	0.18 × 0.16; +67	3.7

Notes. ^(a) Transitions include ortho-NH₃ ($K = 3n$) and para-NH₃ ($K \neq 3n$). ^(b) Energy above the ground reported from the JPL database. ^(c) Synthesized beams in images made with the CASA task CLEAN with a robust parameter set to 0.5. ^(d) RMS noise in a 0.4 km s⁻¹ channel without primary beam correction. After primary beam correction, the noise level increases by up to 25%. ^(e) The $J_K = 13_2-13_1$ line of CH₃OH was detected in the same baseband as the NH₃ (9, 9) line. ^(f) The CH₃CN (2-1) line was observed in a separated baseband paired with the NH₃ (10, 10) line, but was not detected.

the order of 15–25%, depending on transition). Table 1 summarizes the observations.

3. Results

We have mapped the hot NH₃ gas in five highly excited metastable inversion transitions of NH₃ (J, K) = (6, 6), (7, 7), (9, 9), (10, 10), and (13, 13) with 0′.26–0′.19 resolution toward W51 Main. Besides NH₃, we also mapped the $J_K = 13_2-13_1$ line of CH₃OH (with a rest frequency of 27.47253 GHz), while the CH₃CN (2–1) line (with a rest frequency of 36.79371 GHz) was included in our bandwidth but not detected. The parameters of all the observed transitions and the JVLA observations are reported in Table 1. Using the line-free sub-bands, we also produced images of the radio continuum emission with an RMS noise level of ~0.6–0.8 mJy beam⁻¹, at frequencies 25–36 GHz.

In the following we discuss the morphology and velocity field of the molecular gas mapped in hot NH₃ and the CH₃OH line (Sect. 3.1), as well as the spectral profiles of the observed lines (Sect. 3.2).

3.1. Distribution and velocity of hot molecular (NH₃) gas

Figure 1 shows the distribution of hot and dense molecular gas, as traced by the NH₃ (6, 6) line³ with respect to the known HII regions in the W51 Main complex, as traced by the 25 GHz continuum emission (shown with white contours). NH₃ is observed both in absorption (shown with black contours) against the strong HC HII region W51e2-W as well as in emission (shown with cyan contours) in hot gas associated with other dense cores in the region: the dust continuum sources W51e2-E and W51e2-NW (to the east and north of the HC HII region, respectively), and the southern core associated with W51e8. There is no dense gas toward the other HII regions in the cluster; in particular, we do not see dense gas toward the cometary HII region W51e1, which confirms previous results from low-excitation NH₃ transitions (Zhang & Ho 1997).

In order to study the morphology as well as the kinematics of hot molecular gas, we performed a moment analysis deriving

³ The lower excitation line traces best the bulk of the emission from hot molecular gas.

maps of total intensity (0th moment) and velocity field (1st moment), as well as pv diagrams, for each detected transition. In the following, we discuss the results obtained toward each individual source.

3.1.1. The HC HII region W51e2-W

Toward W51e2-W, the NH₃ inversion transitions are observed in absorption and are detected up to the (13, 13) doublet (1700 K above the ground), indicating that there is a significant amount of hot gas presumably still surrounding the HC HII region. Figure 2 shows the total intensity maps (with black contours) superimposed on the intensity-weighted velocity field maps (shown in colors), for all NH₃ transitions as well as the CH₃OH line.

We first consider the morphology of the NH₃ absorption. For lower excitation transitions, NH₃ (6, 6) and (7, 7), as well as the CH₃OH line, we resolve the molecular gas absorption in a central core and an extra component to the SW. A Gaussian fit to the continuum emission from the core provides a deconvolved FWHM size of 0′.27 × 0′.22 (averaged over frequencies which do not display the SW component: 27 to 36 GHz): the core of the HC HII region is therefore not resolved in our maps. Our measurements provide an upper limit to the linear size of the HC HII region of about 1300 AU (at the source distance of 5.4 kpc). The SW extension was previously detected in both continuum emission at 3.6, 1.3, and 0.7 cm (Gaume et al. 1993; Shi et al. 2010a) as well as RLs H26 α , H53 α , and H66 α (Shi et al. 2010a). In particular, Gaume et al. (1993) estimated the spectral indices for both the compact core and the SW extension, finding α of about 2 (optically thick) and 0.4, respectively, and suggested the presence of a one-side (SW) collimated ionized flow emitted from the core. Shi et al. (2010a) used RLs from the cm to submm wavelengths to constrain electron temperatures and densities, and suggested that W51e2 powers both a HC HII core, possibly an ionized disk (see also Keto & Klaassen 2008), and a lower density ionized outflow with a single lobe extended to the SW. This scenario is not inconsistent with our NH₃ observations. The hot and dense material surrounding the HC HII region could in principle be available for accretion onto the central O-type YSO and potentially make up a molecular disk. The SW extension has the weakest integrated absorption and it is not detected in the highest JK transitions, indicating lower temperatures and/or

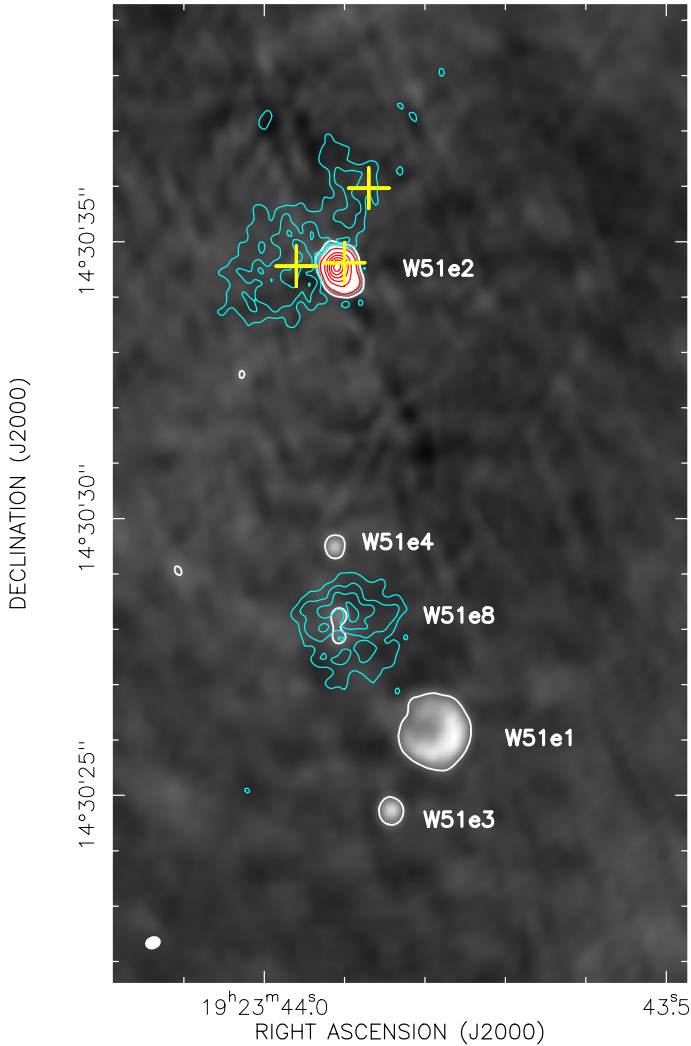


Fig. 1. Distribution of ionized and hot molecular gas in W51 Main as observed with the JVLA-B array. The 25 GHz continuum emission (gray scale and white contours) is produced by the cluster of HII regions W51e1, e2, e3, e4, and e8 (labeled in the plot). The 25 GHz continuum (white) contours indicate 2 mJy flux levels per beam (corresponding to 3σ where $\sigma \sim 0.7$ mJy beam $^{-1}$). The total intensity (0th moment) map of the (6, 6) inversion transition of NH₃ is overlaid on the continuum, showing hot and dense molecular gas toward W51e2 and W51e8. The NH₃ emission is indicated with cyan contours, representing 30% to 90% with steps of 20% of the line peak for the (6, 6) line, 107 mJy beam $^{-1}$ km s $^{-1}$. The NH₃ absorption is indicated with red contours, representing factors 1, 5, 9, 13,.... of -50 mJy beam $^{-1}$ km s $^{-1}$, for all transitions. No flux cutoff was applied. The images were integrated over the velocity range 48 km s $^{-1}$ to 70 km s $^{-1}$, while the velocity resolution was smoothed to 0.4 km s $^{-1}$. The synthesized beam ($0'.29 \times 0'.23$) is shown in the bottom left corner of the panel. The images were constructed with $0'.04$ pixels for all transitions. The yellow crosses around W51e2 indicate the positions of the 0.8 mm continuum peaks identified by Shi et al. (2010a) and correspond to sources W51e2-E, W51e2-W, and W51e2-NW (from left to right), claimed to be individual high-mass YSOs.

densities than the core, as one would expect for outflowing gas. The presence of dense gas to the W and N of W51e2 (see Fig. 1) may explain why the outflow extends only toward the SW. We can use the velocity field maps to establish the nature of the two components.

Perhaps the most striking feature about Fig. 2 is that the NH₃ absorption shows a well-defined velocity gradient in each

line. This gradient appears to change orientation with the excitation line, going from NE-SW for the lower excitation lines, (6, 6) and (7, 7), to E-W for more highly excited lines, (9, 9), (10, 10), and (13, 13). The velocity field of the lower excitation lines, however, is affected by the SW extension, which is blueshifted with respect to the core component and may potentially hide the true sense of rotation in the compact core. Besides the main component, the spectral profile of an NH₃ inversion line displays four symmetric satellite hyperfine components (see Sect. 3.2). Since they are more optically thin and do not display the SW extension, they can reveal the true velocity field more reliably than the main component. Therefore, we created a velocity field map for one of the hyperfine components from the (6, 6) doublet, which has the highest signal-to-noise (S/N). A comparison between the main and the satellite line velocity fields for the (6, 6) doublet is shown in Fig. 3. While the main line shows a velocity gradient oriented NE-SW, the satellite component reveals a velocity gradient oriented E-W (i.e., at a position angle [PA] $\sim 90^\circ$, north to east), consistent with the higher excitation lines. We conclude that the true sense of rotation of the molecular gas is E-W. This is inconsistent with an outflow along SW (see Sect. 5).

Besides 1st moment maps, we also made pv plots of the NH₃ inversion lines. Figure 4 shows an overlay of pv diagrams for the most highly excited lines⁴: $(J, K) = (9, 9)$, $(10, 10)$, and $(13, 13)$. The cuts are taken at the peak of the NH₃ core along the direction of the main velocity gradient observed in the velocity field maps, PA = 90° (E-W). Although a clear velocity gradient is evident in the pv diagrams as well, there is no evidence of steepening of such a gradient with increasing excitation energy (as also displayed in the 1st moment maps).

3.1.2. The W51e2 complex

Figure 5 shows the total intensity images of various NH₃ inversion transitions as well as the CH₃OH line, integrated over their line widths, in the surroundings of W51e2. As already pointed out, while NH₃ is seen in absorption toward the HC HII region (shown with white contours), hot molecular gas is observed in emission (shown with black contours) to the east and to the north of the HC HII region. The structure of the emission from lower excitation lines (e.g., the 6, 6 and 7, 7 NH₃ doublets or CH₃OH) is fairly consistent with the dust emission imaged at 0.8 mm by Shi et al. (2010a; see their Fig. 1), although peaks of warm dust (indicated with crosses in our Fig. 5) and warm ammonia emission do not correspond exactly. Even the most highly excited lines, (10, 10) and (13, 13), show emission (although weak) toward W51e2-E. This demonstrates that W51e2-E is powering a prominent hot core. On the other hand, in the vicinity of the dust peak W51e2-NW, hot NH₃ emission is observed only up to the (9, 9) doublet and it is generally weaker than toward W51e2-E, which indicates lower gas temperature and density (see Sect. 4).

We also created velocity field maps for the NH₃ emission in the W51e2 core. We used the (6, 6) doublet, which has the highest S/N and made velocity maps in both the main component and one of the hyperfine satellites (Fig. 6). Although the velocity field does not show any clear regular pattern, there is an interesting redshifted component near W51e2-E (Fig. 6, top panel), which may indicate infalling gas (see discussion in Sect. 5). Unfortunately this redshifted emission is fairly weak, and we could not detect it in the hyperfine satellites to confirm its nature conclusively (Fig. 6, bottom panel).

⁴ We excluded the lower excitation lines because their velocity fields are affected by the SW component.

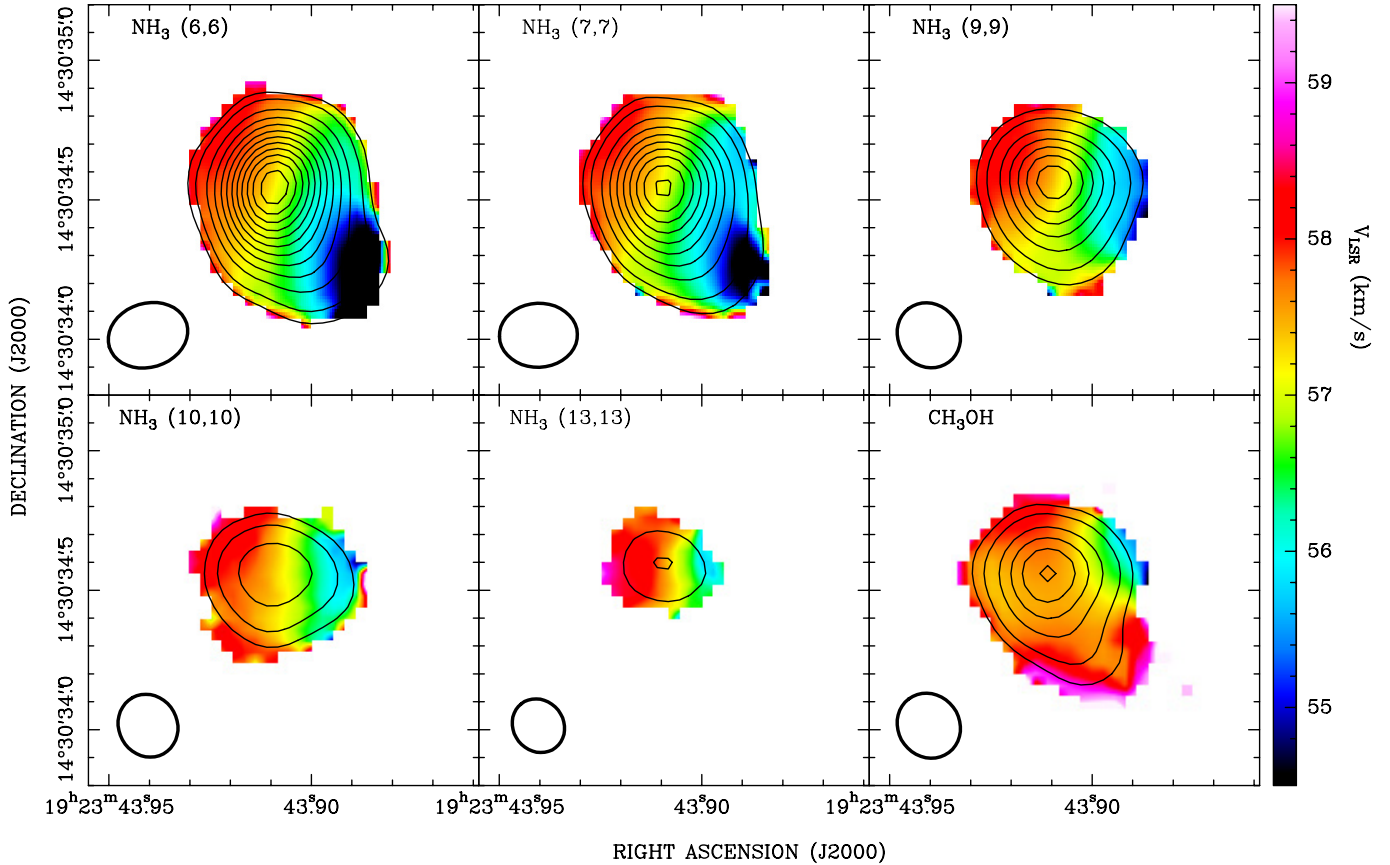


Fig. 2. Velocity fields of five inversion transitions of NH_3 as well as the CH_3OH line, as measured in absorption toward the HC III region W51e2-W with the JVLA B-array. The total intensity 0th moment maps (contours) are overlaid on the velocity field 1st moment maps (images). Colors indicate V_{LSR} in km s^{-1} . The images were constructed with a $0''.04$ pixel for all transitions. The contours represent factors 1, 2, 4, 6, ..., of $-50 \text{ mJy beam}^{-1} \text{ km s}^{-1}$, for all transitions. A flux cutoff of -5 mJy beam^{-1} ($\sim 3\sigma$) was used to create 1st moment maps for the (6, 6), (7, 7), and (9, 9) transitions, and a slightly higher cutoff of -7 mJy beam^{-1} for the (10, 10) and (13, 13) transitions. We note that while the lower excitation transitions (6, 6) and (7, 7) show an apparent velocity gradient along NE-SW, higher excitation lines consistently show a gradient along E-W. We ascribe this difference to a weaker component with blueshifted velocity detected toward SW in the lower excitation lines. The synthesized beams ($0''.19$ – $0''.26$) are shown in the bottom left corner of each panel (see Table 1).

In order to better examine any potentially regular velocity pattern in the molecular gas surrounding W51e2-E, we made a pv diagram for the (6, 6) doublet, which again has the highest S/N, shown in Fig. 7. The cut is taken at the presumed position of the protostar, which we assume is coincident with the peak of the (13, 13) NH_3 emission (see also Sect. 5), and at $\text{PA} = 45^\circ$, i.e., perpendicular to the axis of the known CO outflow (see Fig. 14 and Shi et al. 2010b). From the pv plot, there is no evidence for a velocity gradient that may indicate gas rotation. Nevertheless, the pv diagram shows a C-shaped structure (in the blueshifted side) as well as an O-shaped structure (when the redshifted side is also included; although this feature is less clear). This pattern is expected for a radially infalling core, where the l.o.s. velocity displacement is expected to be maximum at the center and then to decrease away from it. An expanding shell or a wide-angle outflow cannot be completely ruled out, however. An interpretation of this pattern is given in Sect. 5.

3.1.3. The W51e8 core

Figure 8 shows the total intensity images of various NH_3 inversion transitions and the CH_3OH line toward W51e8. The emission shows a stronger central component, which is elongated E-W across $\sim 2''$ and is detected in all transitions and a more diffuse, nearly spherical core surrounding the central component, which is detected only at lower excitation. This indicates

temperature variations within the core with the lower JK doublets tracing the cooler parts of the NH_3 core.

We also created velocity field maps for both the main hyperfine line and one of the hyperfine satellites from the (6, 6) doublet (see Fig. 9). Although the velocity field looks somewhat complex, it is still possible to discern some regular patterns. For example, redshifted emission is almost exclusively located in the SE, while the emission to the west and north are mildly blueshifted; the lowest blueshifted velocity is located to the SW. Therefore, the velocity field map suggests two directions with potential velocity gradients in the molecular gas surrounding W51e8: E-W and N-S. We made pv diagrams of the (6, 6) doublet at $\text{PA} = 0^\circ$ and $\text{PA} = 90^\circ$ to confirm their presence more confidently (bottom and top panels of Fig. 10, respectively). The cuts were taken at the peak of the 25 GHz continuum emission, which also corresponds to the peak of the (13, 13) NH_3 line; this is the presumed location of the exciting protostar; see Sect. 5. Although the structure is not symmetric with respect to the zero position, these pv plots support the presence of two velocity gradients in perpendicular directions.

3.2. Spectral profiles

We extracted spectral profiles toward individual sources by mapping each spectral channel and summing the flux density in each channel map for each transition. Figures 11–13 show such

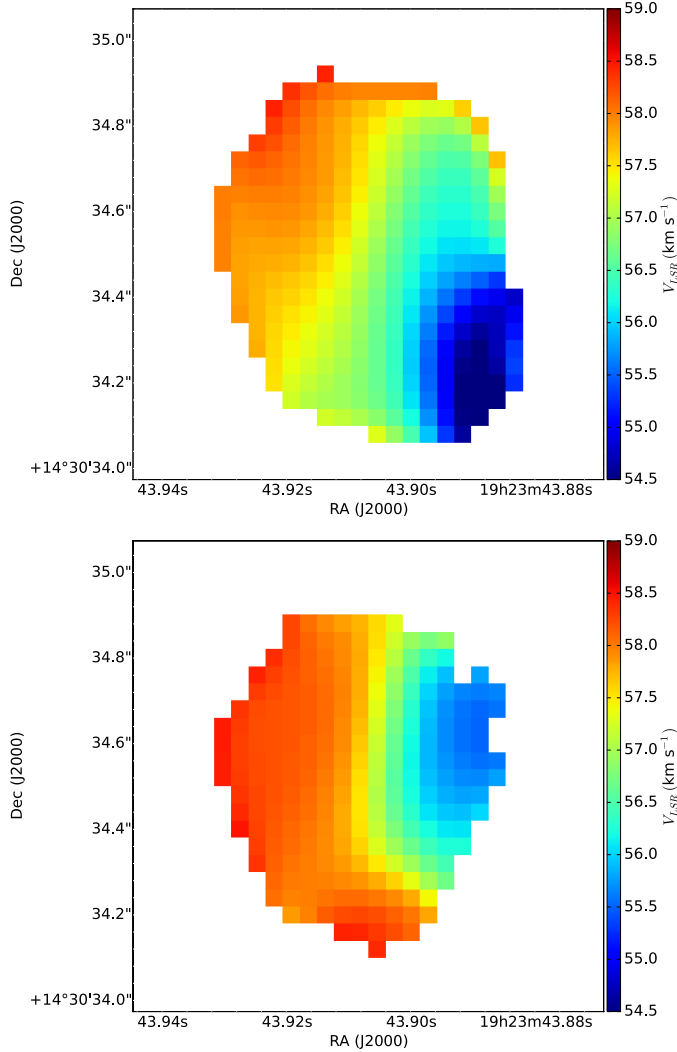


Fig. 3. Velocity field of the NH_3 (6, 6) inversion line for both the main line (*top panel*) and one of the satellite components (*bottom panel*), as fitted toward the HC HII region W51e2-W with the JVLA B-array. The images were constructed with $0''.04$ pixels. Colors indicate V_{LSR} in km s^{-1} (color bar). The main component has an apparent velocity gradient along NE-SW, whereas the true velocity gradient displayed by the satellite component is along E-W (see text). The velocity field maps were created by fitting the data cube (channel-by-channel) using *pyspeckit* (Ginsburg & Mirocha 2011).

spectral profiles extracted toward the W51e2-W HC HII region, and the sources seen in NH_3 emission in the W51e2 core and the W51e8 core, respectively. As displayed in these plots, the NH_3 profiles are not simply composed of a single spectral component. In fact, owing to the interaction with the quadrupole moment of the nitrogen nucleus, each NH_3 inversion line is actually split into five components, a “main component” and four symmetrically spaced “satellites”, which make up the NH_3 hyperfine structure (HFS). The frequency separations and relative intensities of the four satellite components can be calculated using quantum mechanics formalism for a symmetric molecular rotor (see Appendix B for the relevant equations); these parameters are reported in Table 3 (at least for the lines observed in this study). The satellite lines are spaced $\sim 27\text{--}31 \text{ km s}^{-1}$ from their main components, so they are well resolved from each other.

The entire HFS spectra for the observed NH_3 inversion lines are shown in the left panels of Figs. 11–13, whereas the middle

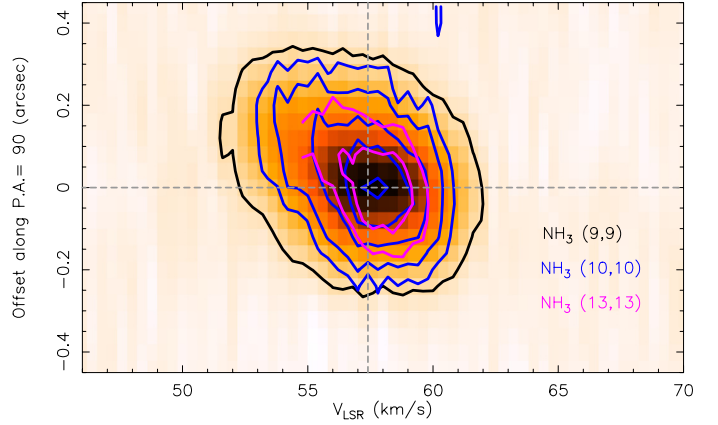


Fig. 4. Overlay of position-velocity diagrams of the $(J, K) = (9, 9)$, $(10, 10)$, $(13, 13)$ lines observed with the JVLA B-array toward W51e2-W. The cut is taken at the peak of the NH_3 core with a PA = 90° . The image shows the pv diagram for the $(9, 9)$ doublet. The contours are $-0.005 \text{ Jy beam}^{-1}$ for the $(9, 9)$ transition (in black), $-0.005, -0.01, -0.02, -0.03, -0.04 \text{ Jy beam}^{-1}$ for the $(10, 10)$ transition (in blue), -0.005 and $-0.01 \text{ Jy beam}^{-1}$ for the $(13, 13)$ transition (in magenta), respectively. The vertical dashed gray line indicates the velocity at 57.4 km s^{-1} . The PA is measured from north to east.

and right panels show the profiles of the NH_3 main central hyperfine components and the CH_3OH line, respectively, in more detail. Individual spectral profiles do not show the presence of multiple velocity components, so they can be reasonably well fitted by single Gaussian profiles.

In order to derive the line parameters, we used five-component Gaussian models to fit the HFS in each of those inversion transitions, where we fixed their velocity separations according to the calculated values, assuming the same line widths for all four hyperfine components to reduce the number of free parameters. In order to derive the kinematics in optically thin lines, we also fit the hyperfines only with a four-component Gaussian model again with fixed offsets and line widths. The fitted line parameters are reported in Table 2 for the main components and in Table 3 for the hyperfine components⁵.

In the following, we describe properties of spectral profiles in individual sources.

3.2.1. The HC HII region W51e2-W

The absorption spectral profiles for both the NH_3 and CH_3OH transitions are shown in Fig. 11. Gaussian fitting provides similar central velocities, $V_c = 57.1\text{--}57.5 \text{ km s}^{-1}$, for multiple transitions of NH_3 , from (6, 6) to (13, 13), but very different FWHM line widths, $\Delta V_{1/2} = 3.9\text{--}7.2 \text{ km s}^{-1}$ (see Table 2). We do not believe this is a physical effect, and we ascribe the larger line widths (as well as the slightly lower central velocities) inferred for the lower excitation lines to their higher opacities. In fact, perhaps the most striking feature of the NH_3 spectral profiles shown in the left panel of Fig. 11 is the prominence of the two pairs of hyperfine satellites, which reach a relative intensity with respect to the main component of nearly 50%, indicating extreme optical depth values (see last column of Table 3).

⁵ Since we did not manage to obtain good fits to the absorption in the most optically thick lines (6, 6) and (7, 7) with the multi-Gaussian models, we also attempted a fit using models that account for the optical depth of the main and hyperfine components (see Sect. A.3).

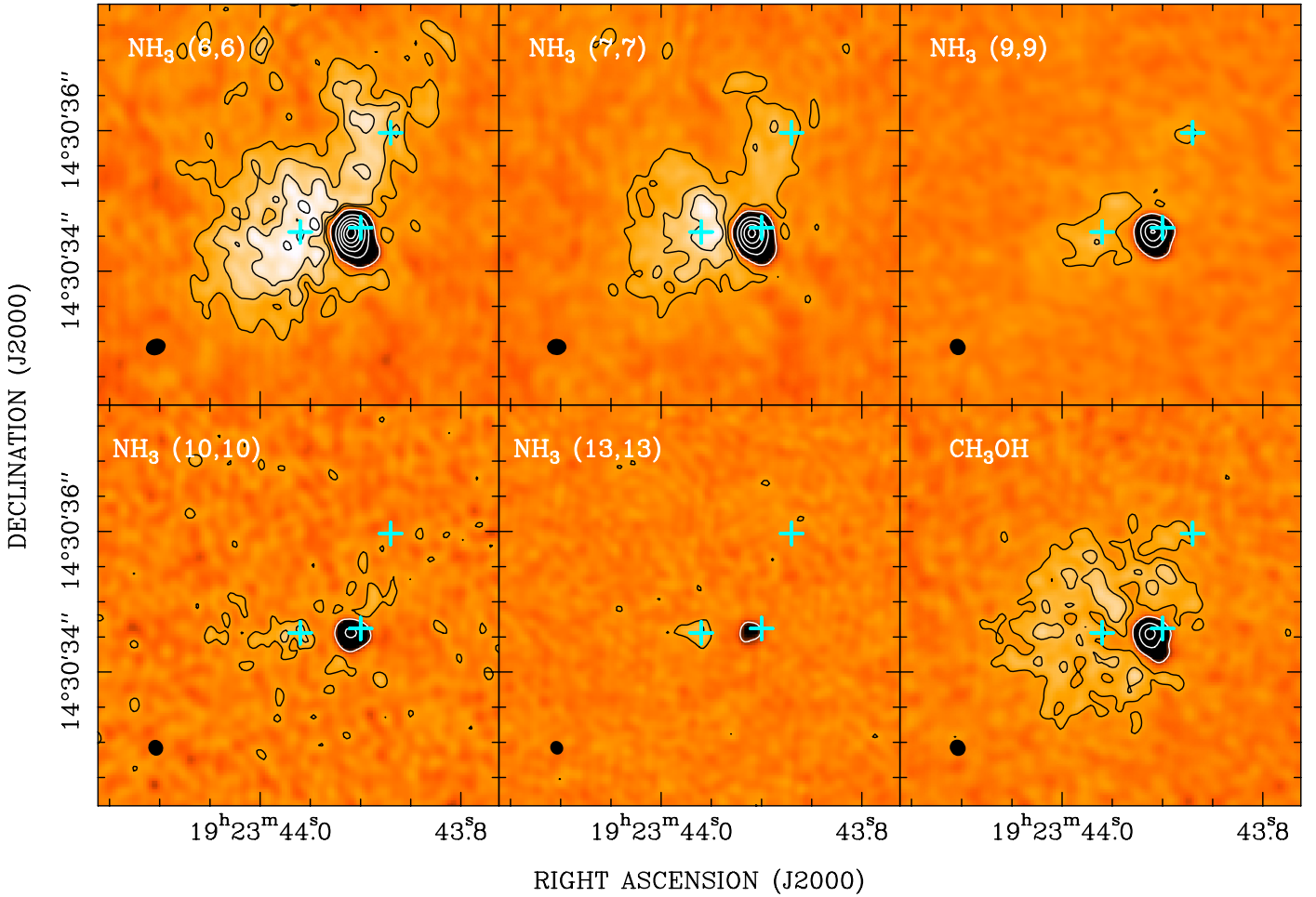


Fig. 5. Total intensity images of five inversion transitions of NH_3 as well as the CH_3OH line toward W51e2. Light colors indicate emission and dark colors absorption. Contours of the NH_3 total intensity are also overplotted in the image: emission is displayed with black contours, representing factors 1, 2, 3, 4,.... of $20 \text{ mJy beam}^{-1} \text{ km s}^{-1}$; absorption is displayed with white contours, representing factors 1, 5, 9, 13,.... of $-50 \text{ mJy beam}^{-1} \text{ km s}^{-1}$, for each transition, respectively. The images were integrated over the velocity range covering the main hyperfine component for each transition (from 48 km s^{-1} to 70 km s^{-1}). The velocity resolution was smoothed to 0.4 km s^{-1} for all transitions. The synthesized beams ($0''.19\text{--}0''.26$) are shown in the bottom left corner of each panel (see Table 1). The images were constructed with $0''.04$ pixels for all transitions. The cyan crosses mark the positions of the 0.8 mm continuum peaks identified by Shi et al. (2010a) and corresponding to sources W51e2-E, W51e2-W, and W51e2-NW (from left to right), claimed to be individual high-mass YSOs.

When we fit line widths and opacities simultaneously (see Sect. A.3), we derive similar line widths for the main hyperfine components at different excitation of about 4 km s^{-1} . This value is consistent with the parameters fitted for the hyperfine satellites in the (6, 6) and (7, 7) doublets, which are expected to be more optically thin than the main line. Likewise, we consider that the central velocities estimated from the hyperfine satellites are more reliable than the main component. In conclusion, for the NH_3 core associated with the HC HII region W51e2-W, we infer a systemic velocity of 57.4 km s^{-1} and a line width of 4.4 km s^{-1} (see Table 3).

3.2.2. The W51e2-E and NW sources and surrounding core

We extracted spectra toward W51e2-E and W51e2-NW⁶, as well as across the whole core, defined by the region where the NH_3 (6, 6) inversion line is observed in emission (Fig. 5). These spectra are shown in Fig. 12 (top, middle, and bottom panels, respectively). All spectra show prominent satellites in the lower

⁶ The positions and radii defining the areas where the spectra were integrated are reported in Table 2.

excitation lines, indicating high optical depths. This is reflected in the very different values estimated for the central velocities and line widths for different excitation lines (see Table 2).

Owing to their symmetry, the optically thin lines unambiguously define the systemic velocity of the core. Therefore, to derive central velocities and line widths, we again rely on the more optically thin hyperfine satellites: 56.4 , 55.2 , 55.3 km s^{-1} , and 9.3 , 8.7 , 9.3 km s^{-1} for the W51e2-E and W51e2-NW sources and the entire W51e2 core, respectively.

3.2.3. W51e8

For W51e8, we integrated across an approximately spherical region (with a radius of $3''.7$) where the NH_3 (6, 6) inversion line is observed in emission (Fig. 8). The spectral profiles are shown in Fig. 13. We derive central velocities varying in the range 58.5 to 60.6 km s^{-1} and line widths in the range $7.5\text{--}13 \text{ km s}^{-1}$ from multiple transitions of NH_3 as well as the CH_3OH line. From the hyperfine satellites detected from the (6, 6) and (7, 7) doublets, we infer a consistent systemic velocity of $\sim 60 \text{ km s}^{-1}$, but their line widths remain fairly uncertain in the range $8\text{--}14 \text{ km s}^{-1}$.

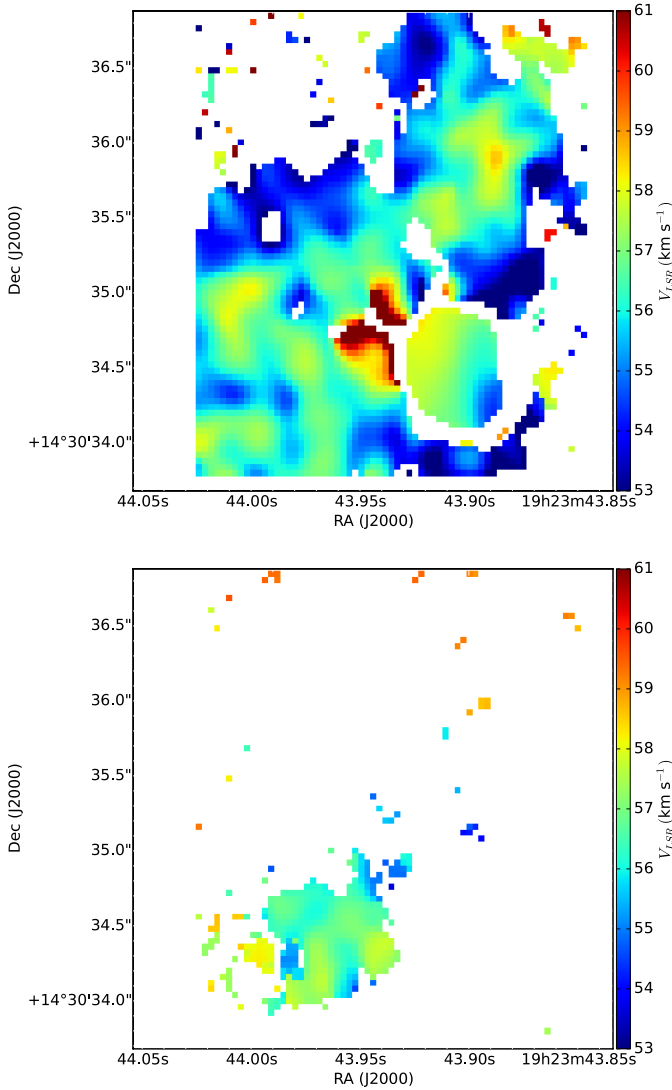


Fig. 6. Velocity field of the NH_3 (6, 6) inversion line for both the main line (*top panel*) and one of the satellite components (*bottom panel*), as measured in the W51e2 complex. The images were constructed with $0''.04$ pixels. Colors indicate V_{LSR} in km s^{-1} from 53 to 61 km s^{-1} by 0.4 km s^{-1} (color bar).

We conclude that W51e8 is significantly redshifted with respect to the W51e2 core, and has a large internal velocity dispersion (probably $>10 \text{ km s}^{-1}$), possibly indicating very turbulent and/or outflowing gas (see discussion in Sect. 5).

4. Analysis: determining physical conditions

NH_3 is a high-density gas tracer and its inversion lines provide an excellent probe of the gas kinetic temperature (Ho & Townes 1983). Using the parameters measured for the HFS of the five NH_3 inversion transitions observed in W51 Main and in the assumption of LTE (i.e., the metastable inversion lines are thermalized), we can estimate the physical conditions of the NH_3 gas such as optical depth (τ), rotational temperature (T_{rot}), and column density (N_{col}). The methodology, as well as the formalism adopted to analyze the NH_3 data, are described in Appendix A.

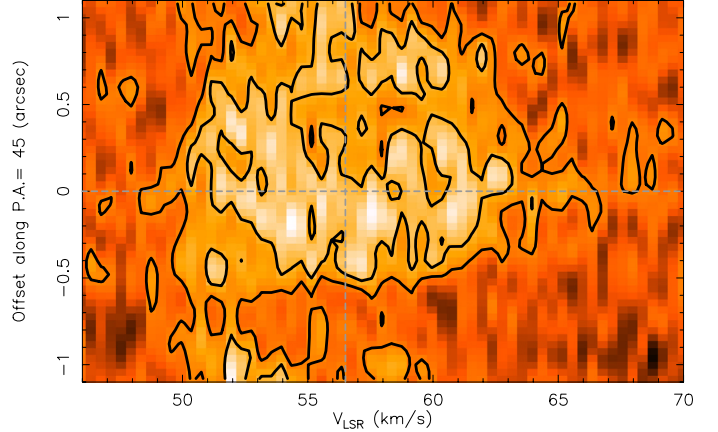


Fig. 7. Position-velocity diagram of the $(J, K) = (6, 6)$ line observed in emission around the protostar W51e2-E. The cut is taken at the presumed location of the protostar (see text) with a PA = 45° (north to east). The contours are 0.005 and $0.01 \text{ Jy beam}^{-1}$. The vertical dashed gray line indicates the velocity at 56.4 km s^{-1} .

We detected hyperfine pairs of satellite lines for the (6, 6), (7, 7), and (9, 9) transitions toward cores e2-W, e2-E, e2-NW⁷, and e8 (Table 3). In particular, the hyperfine satellites are remarkably prominent in the (6, 6) doublet, where they show relative intensities (with respect to the main line) from roughly 50% to nearly 100% toward cores e2-W and e2-E, respectively (see Figs. 11 and 12). The expected theoretical value of the ratio of the satellite to the main component strengths of the lines targeted here is $<1\%$ assuming LTE (see Col. 6 in Table 3), indicating very large optical depths even for these highly excited transitions. Indeed, the values of optical depths that we derive vary in the range 10–100 from the (9, 9) down to the (6, 6) line (see Table 3), indicating exceptionally high opacity in the gas seen both in absorption and emission. The W51e2-E core is the most optically thick and the W51e8 core is the least optically thick.

After estimating the optical depths, we used rotational temperature diagrams (RTDs) to derive rotational temperature and column densities of the NH_3 gas toward all the cores (see description in Appendix A and Figs. A.1, A.2). Since we do not have direct estimates of the opacity for all transitions, and we cannot exclude that even the most highly excited transitions are optically thick, we used only the transitions (6, 6), (7, 7), and (9, 9) in our analysis of the physical conditions. We estimated an average rotational temperature of 140 K for the W51e2 complex, which rises to 174 K, 173 K, and 144 K for the individual cores e2-W, e2-E and e2-NW, respectively. For W51e8, we estimated a slightly higher temperature of about 200 K. Using an RTD analysis with CH_3CN lines at 2 mm, Zhang et al. (1998) found rotation temperatures of 140 K and 130 K, while Remijan et al. (2004) estimated 153 K and 123 K using CH_3CN transitions at 3 mm and 1 mm for W51e2 and W51e8, respectively. While these previous estimates for W51e2 are consistent with our estimates, the lower temperatures inferred for W51e8 could be ascribable to a temperature gradient and to the coarser angular resolution ($1\text{--}3''$) of previous observations⁸.

For the column density, we can only make a reliable estimate for the absorption against the HII region, where the good S/N in both the main and satellite spectral components enabled

⁷ The (9, 9) doublet was not detected in W51e2-NW.

⁸ In W51e2 we find that the gas temperature in different cores is the same within 30 K, so the impact of different angular resolutions on the temperature estimates should be less important than for W51e8.

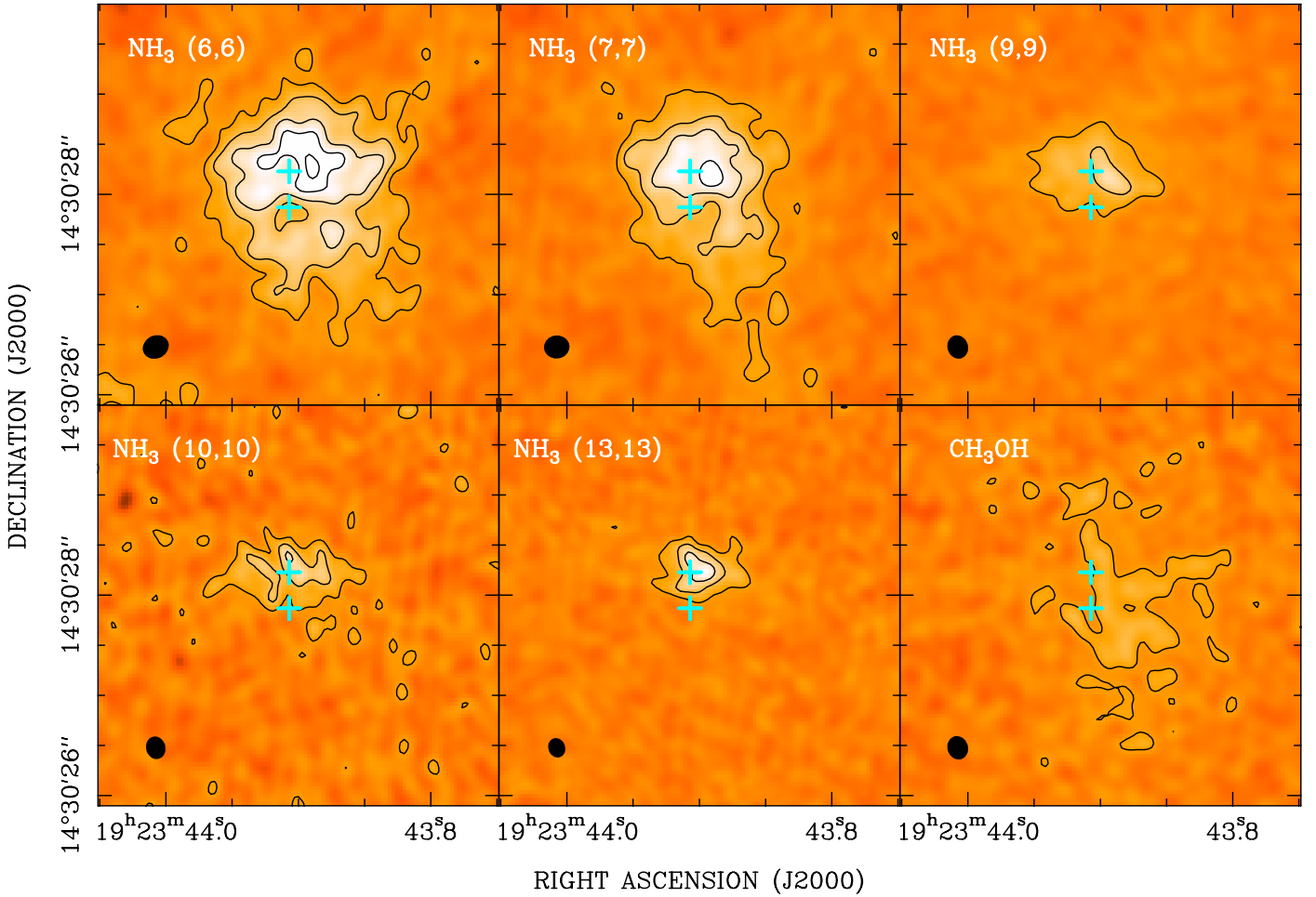


Fig. 8. Total intensity images of five inversion transitions of NH_3 as well as the CH_3OH line toward W51e8. Contours of the NH_3 total intensity are also overplotted in the image, representing factors 1, 2, 3, 4,.... of $20 \text{ mJy beam}^{-1} \text{ km s}^{-1}$. The images were integrated over the velocity range covering the main hyperfine component for each transition (from 48 km s^{-1} to 70 km s^{-1}). The velocity resolution was smoothed to 0.4 km s^{-1} for all transitions. The synthesized beams ($0'.19$ – $0'.26$) are shown in the bottom left corner of each panel (see Table 1). The images were constructed with $0'.04$ pixels for all transitions. Note that ammonia emission is detected toward W51e8 up to the (13, 13) doublet. The cyan crosses mark the positions of the radio continuum peaks identified at 25 GHz (see Fig. 1).

accurate estimates of the gas opacity. For the gas seen in emission, where our opacity estimates have large error bars, we provide only lower limits to the true column density (assuming optically thin gas). After estimating the NH_3 column density, we can calculate the volume density and total mass of the molecular gas in each individual core in W51 Main. In this calculation, we assume an ammonia fractional abundance of $[\text{NH}_3]/[\text{H}_2] = 10^{-7}$ (e.g., [Mauersberger et al. 1986](#))⁹ and a spherical gas distribution within the core radius. The latter corresponds to approximately the average between the semi-major and semi-minor axes of the ellipse used to integrate the spectra in each core (see Table 2), except for the absorption in the HC HII region. Since the HC HII region is not resolved in our maps, we take as an upper limit 320 AU to its radius ($0'.06$; [Shi et al. 2010a](#)). According to this analysis, for the molecular gas surrounding the HC HII region

⁹ We explicitly note that the value of $[\text{NH}_3]/[\text{H}_2]$ is known to no better than an order of magnitude, therefore the values of mass and molecular density are just order-of-magnitude estimates. In addition, this ratio is fixed, therefore our analysis neglects the effect of chemistry on the location and abundance of ammonia molecules within W51 Main. For a model with variable fractional abundance, please see [Osorio et al. \(2009\)](#).

we derive a volume density of $\sim 6.9 \times 10^9 \text{ cm}^{-3}$ and an upper limit to the molecular mass of about $5 M_\odot$.

For the entire core e2, which surrounds the HC HII region and is seen in NH_3 emission, we derive lower limits to both the volume density ($\sim 3 \times 10^6 \text{ cm}^{-3}$) and the gas mass ($\sim 80 M_\odot$). The density increases toward the positions of the dusty sources W51e2-E and W51e2-NW, where we estimate (lower limits to the) gas masses of $18 M_\odot$ and $32 M_\odot$ within about half an arcsecond and one arcsecond from the two sources, respectively. For W51e8, we estimate a gas density of $\sim 3 \times 10^6 \text{ cm}^{-3}$ and a gas mass of about $70 M_\odot$, which is similar to the entire W51e2 core. Unlike the latter, however, we do not see evidence of multiple sources in W51e8 besides central condensation. Our estimates are slightly lower than but overall consistent with the values for the gas mass derived by [Hernández-Hernández et al. \(2014\)](#) from 1.3 mm continuum dust emission imaged with the SMA at $\geq 1''$ resolution (96 and $86 M_\odot$, for W51e2 and W51e8, respectively).

5. Discussion

We have identified two main centers of HMSF activity in W51-Main, which excite hot cores and presumably host one or multiple high-mass YSOs at their centers: the W51e2 complex

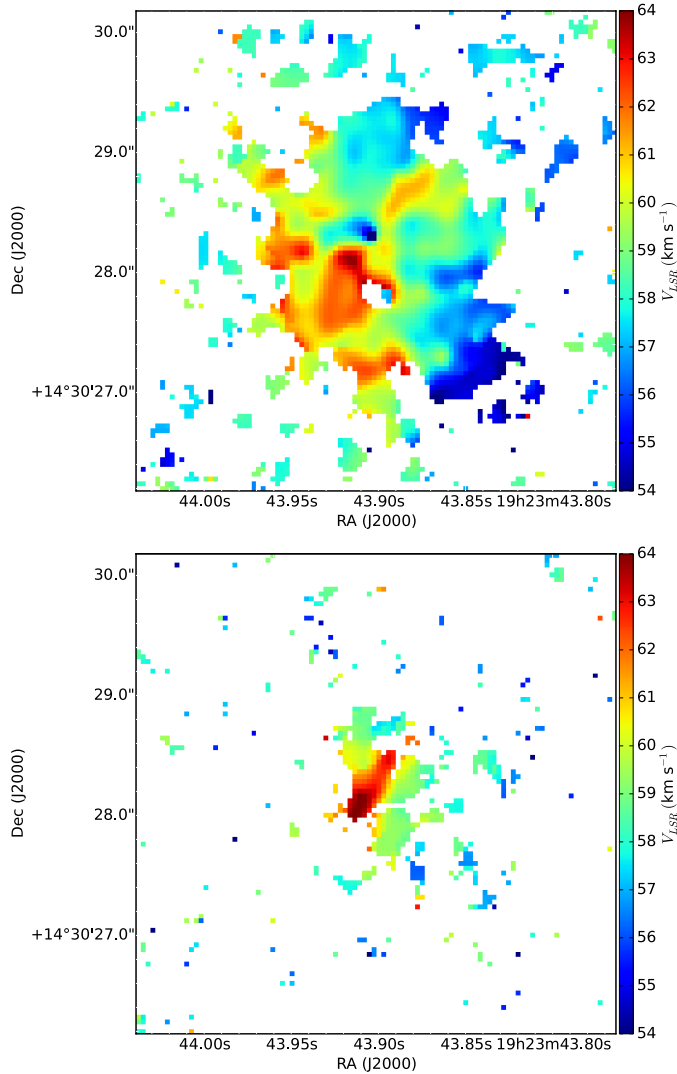


Fig. 9. Velocity field of the NH_3 (6, 6) inversion line for both the main line (*top panel*) and the satellite components (*bottom panel*), as measured in emission toward W51e8. Colors indicate V_{LSR} in km s^{-1} (color bar). The images were constructed with $0''.04$ pixels.

(forming a multiple system) and the W51e8 core ($\sim 6''$ southward of W51e2). We analyze our NH_3 maps in the context of previously published high-resolution data to characterize the nature of these hot cores and their exciting sources and more generally assess the star formation activity in W51 Main. The main physical and kinematic properties of the identified high-mass YSOs and/or hot cores in W51 Main are summarized in Table 4.

5.1. The W51e2 complex

We present here a series of overlays of our NH_3 images with different star formation tracers in the W51e2 complex. In particular, Fig. 14 shows an overlay of the CO $J = 3-2$ 0th moment image from the SMA (blue and red contours; Shi et al. 2010b) onto the total intensity (0th moment) map of the (6, 6) inversion transition of NH_3 (with white contours showing emission and black contours showing absorption). Figures 15–17, show the same (6, 6) NH_3 total intensity map with overlaid different molecular maser

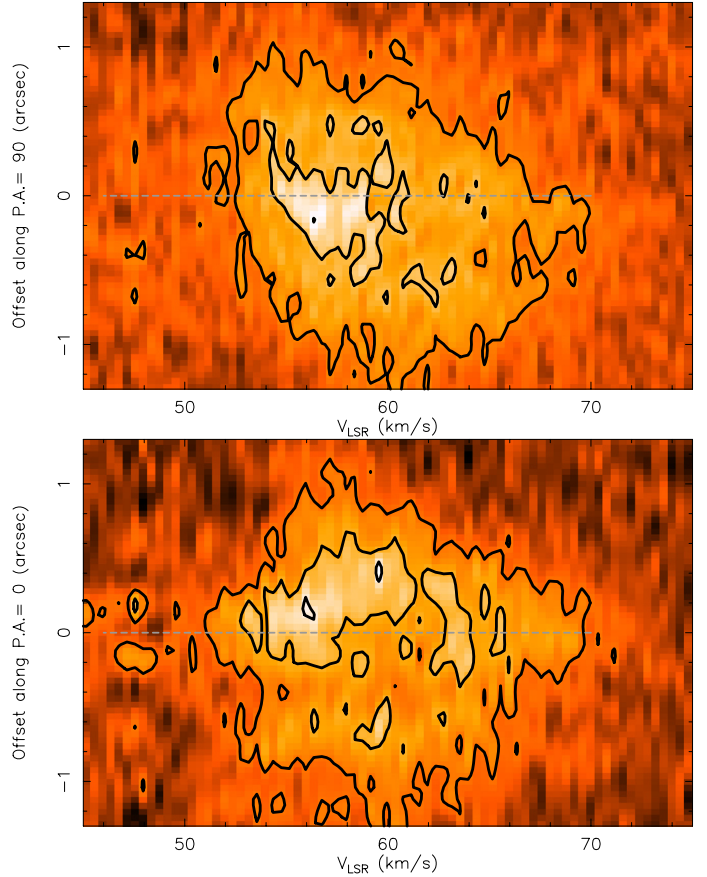


Fig. 10. Position-velocity diagram of the $(J, K) = (6, 6)$ line observed in emission around the protostar W51e8. The cut is taken at the presumed location of the protostar (see text) with a $\text{PA} = 90^\circ$ (*top panel*) and $\text{PA} = 0^\circ$ (*bottom panel*). The PA is measured from north to east. The contours are 0.002 and 0.004 Jy beam^{-1} .

species (CH_3OH , H_2O , OH) detected around W51e2¹⁰. In the following, we discuss physical properties of each of the three cores: W51e2-E, W51e2-W, and W51e2-NW.

W51e2-E. Figure 14 reveals a core of dense hot molecular gas at the center of the CO outflow and clearly shows that the driver of the CO outflow is not the HC HII region, but the dusty source W51e2-E (as first noticed by Shi et al. 2010b). Interestingly, we find that the peak of the total intensity map of the most highly excited (13, 13) NH_3 transition (shown with the cyan contour), presumably locating the hottest gas, falls at the center of the blueshifted and redshifted lobes of the outflow. Therefore, we assume that this peak locates the position of the embedded protostar driving the CO outflow, i.e., W51e2-E. Shi et al. (2010b) derived a mass-loss rate of $10^{-3} M_\odot \text{ yr}^{-1}$ and a mechanical power of $120 L_\odot$, which is an order of magnitude larger than expected for an early B-type star (e.g., Arce et al. 2007).

¹⁰ We choose the (6, 6) ortho-transition as a standard for the NH_3 dense gas distribution because it is the strongest among the observed transitions. We do not believe this introduces a bias due to e.g. differences between ortho and para-species or the possibility of maser emission. Indeed, the (6, 6) emission displays a morphology similar to the strongest observed para-transition (7, 7) (see Fig. 5). We also believe that the (6, 6) emission is unlikely to be masing given that it is apparently consistent with the other lines (assuming a single LTE temperature) and given that there are no narrow, extremely bright features in the spectral profiles; see, for example, Figs. 3 and 4 of Paper II for an example of NH_3 (6, 6) maser line in W51 north.

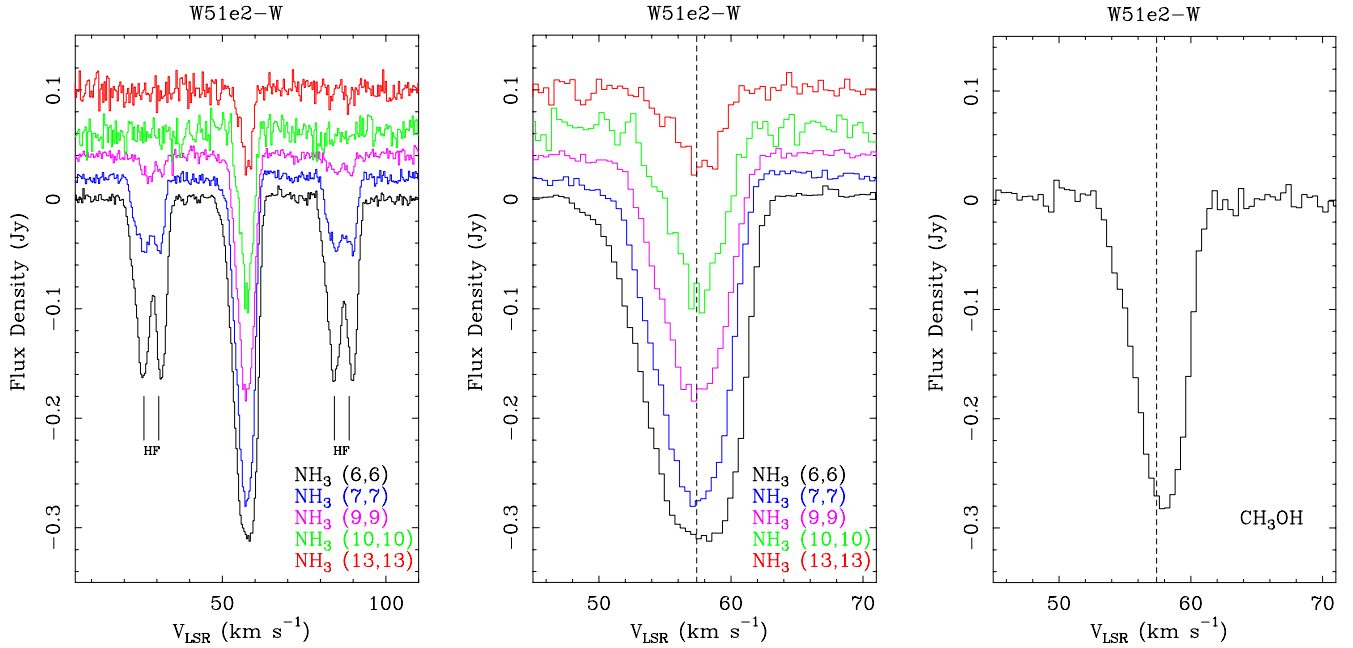


Fig. 11. Spectral profiles of the absorption lines integrated over the radio continuum emission in W51e2-W. *Left and central panels:* spectral profiles of NH_3 for transitions (6,6), (7,7), (9,9), (10,10), and (13,13). An offset in flux density is applied to transitions adjacent in energy to better display individual profiles. The lower state energy levels of transitions shown here are $\sim 408\text{--}1691$ K (see Table 1). The hyperfine satellite lines, separated by $\sim \pm 24\text{--}31$ km s^{-1} (see Table 3), are clearly detected for the (6,6), (7,7), and (9,9) lines (*left panel*). A narrower velocity range is plotted in the *central panel* to show the line profiles of the main hyperfine component of each inversion transition more clearly. *Right panel:* spectral profile of the $J_K = 13_2\text{--}13_1$ line of CH_3OH ($\nu_{\text{rest}} = 27.473$ GHz). The velocity resolution is 0.4 km s^{-1} (*all panels*), and the vertical dashed line indicates a velocity of 57.4 km s^{-1} (*central and right panels*).

This finding suggests that the protostellar core W51e2-E is forming an O-type star. Alternatively, a cluster of B-type stars could in principle explain the high mechanical power but would not be expected to drive a collimated outflow and therefore can be excluded in this case. Based on dust emission, Shi et al. (2010a) estimated $140 M_{\odot}$ available in the whole core. We estimate nearly $20 M_{\odot}$ of gas (assuming $[\text{NH}_3]/[\text{H}_2] = 10^{-7}$) within about half an arcsecond from the presumed location of the protostar, indicating a significant amount of material in the immediate vicinity of the protostar available for accretion.

Aside from large mass and powerful outflow, another indication of the presence of a high-mass protostar is provided by the excitation of CH_3OH , H_2O , and OH masers around W51e2-E (Fig. 15). In particular, Class II CH_3OH masers are interesting because they are a typical signpost for HMSF. Etoka et al. (2012) used MERLIN to show that the bulk of methanol maser emission comes from a compact ($\sim 0''.5$) ring-like structure centered approximately at the (13,13) NH_3 emission peak (Fig. 15, top panel). Besides the ring, masers are also distributed to the NE and SW of the ring, across $1''.5$, and show a clear velocity coherence, with blueshifted emission to the SW and redshifted emission to the NE, for a total velocity extent of about 10 km s^{-1} . Since this structure is roughly perpendicular to the CO outflow ($\text{PA} \sim 150^\circ$), a natural explanation could be that it traces an accretion flow; the structure across $1''.5$ could be an infalling envelope and the central ring (within $0''.5$) may probe a compact and dense disk or torus around the central protostar. Accretion however is not the only possibility. An alternative interpretation would be that the red and blueshifted maser components are diverging from W51e2-E with an expansion velocity of ~ 5 km s^{-1} , tracing a slow and episodic wide-angle outflow along NE-SW (in this scenario, the central ring would indicate a younger outflow event).

H_2O masers show a bipolar structure along NW-SE, with redshifted velocities to the NW and blueshifted velocities to the SE (Fig. 15, middle panel) in agreement with the CO emission. Sato et al. (2010) measured their proper motions, clearly identifying a fast outflow ($V_{\text{exp}} = 120 \pm 12$ km s^{-1}) arising from W51e2-E along NW-SE (Fig. 16, top panel), i.e., perpendicular to the CH_3OH maser distribution and along the more extended molecular outflow seen in the CO (3–2) line (Shi et al. 2010b).

Finally, Fish & Reid (2007) observed several transitions of OH masers at 1.7 GHz with the VLBA and measured their positions, l.o.s. velocities, and proper motions (Fig. 17 and bottom panel of Fig. 15). The OH masers appear to be distributed in two main clusters. The first cluster is associated with W51e2-E and is distributed along the CO outflow with redshifted spots to the NW and blueshifted to the SE accordingly; these may be tracing the innermost portion of the outflow, along with the H_2O masers, at least based on positions and l.o.s. velocities. Proper motions seem to show a more complex kinematic structure, although they seem to globally indicate a wide-angle expansion around W51e2-E (at much lower velocity than the H_2O masers, however). Interestingly, there are quite a few redshifted spots that have velocity vectors pointing inward toward W51e2-E; these may potentially probe infalling gas. The second cluster is excited south of the HC HII region, where OH masers (along with few CH_3OH masers) arise in two groups located in correspondence with the contours of hot NH_3 gas engulfing the HII region to the south. It is not clear whether these OH masers are associated with W51e2-E, with the HC HII region, or are excited by a third (undetected) source. Likewise, their kinematics is rather unclear, although they seem to have proper motions diverging from W51e2-E.

In summary, these high-angular resolution measurements of molecular masers provide convincing evidence of a fast

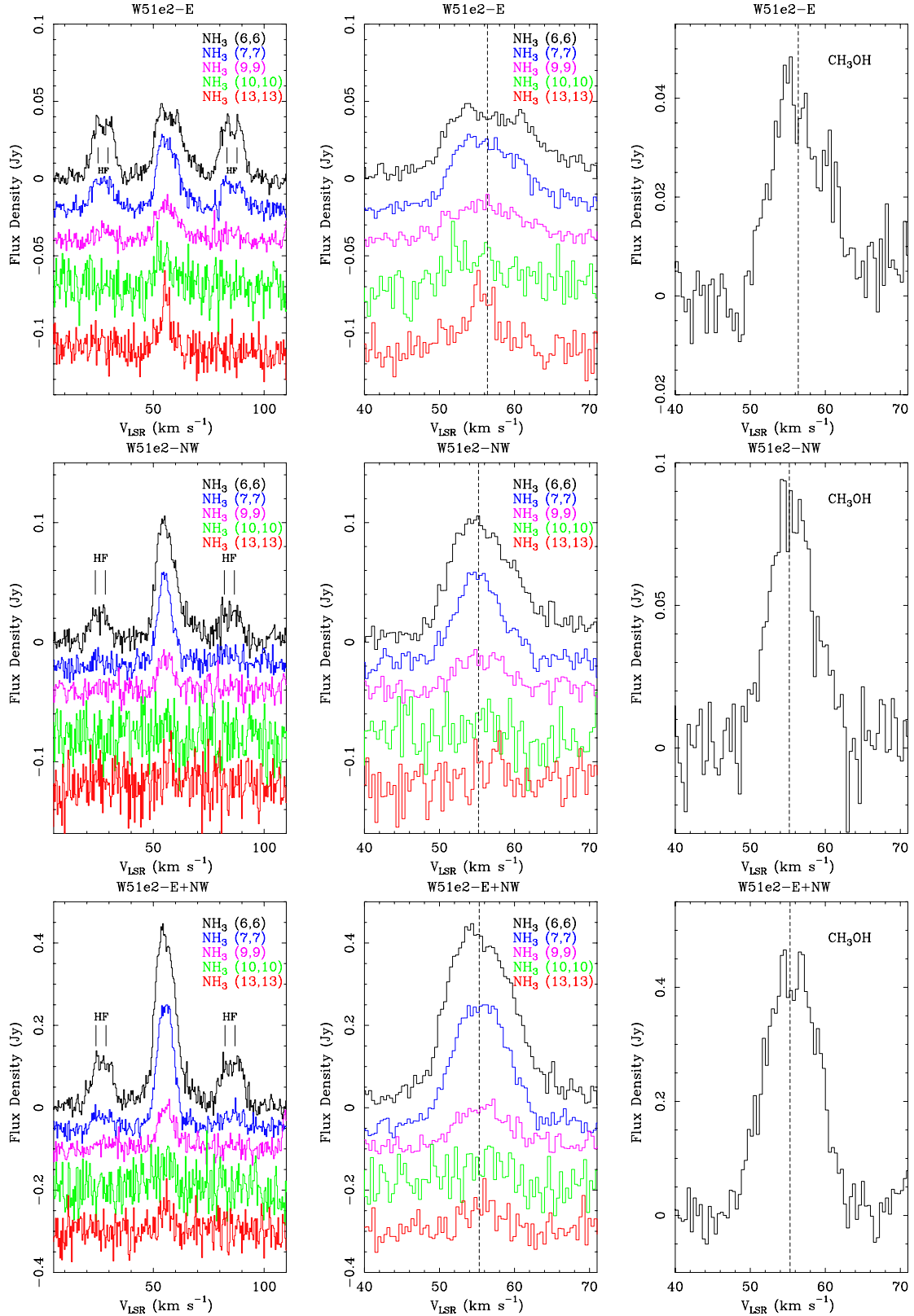


Fig. 12. Spectral profiles of emission lines arising from hot molecular gas in the surroundings of the HC HII region. The spectra shown are integrated toward the dust continuum sources W51e2-E (*top row*), W51e2-NW (*middle row*), and toward the entire molecular core seen in emission (*bottom row*), respectively. *Left and central panels*: spectral profiles of NH_3 for transitions (6, 6), (7, 7), (9, 9), (10, 10), and (13, 13). An offset in flux density is applied to transitions adjacent in energy to better display individual profiles. The lower state energy levels of transitions shown here are $\sim 408\text{--}1691$ K (see Table 1). The hyperfine satellite lines, separated by $\sim \pm 24\text{--}31$ km s $^{-1}$ (see Table 3), are clearly detected for the (6, 6), and (7, 7) doublets in the three cases; the (9, 9) HF lines are detected only toward W51e2-E (*top row, left panel*). A narrower velocity range is plotted in the *central panel* to show the profiles of the main hyperfine component of each inversion transition more clearly. *Right panel*: spectral profile of the $J_K = 13_2\text{--}13_1$ line of CH_3OH ($\nu_{\text{rest}} = 27.473$ GHz). The velocity resolution is 0.4 km s $^{-1}$ (*all panels*), and the vertical dashed line in the *central and right panels* indicate velocities of 56.4 km s $^{-1}$ (*top row*), 55.2 km s $^{-1}$ (*middle row*), and 55.3 km s $^{-1}$ (*bottom row*), respectively.

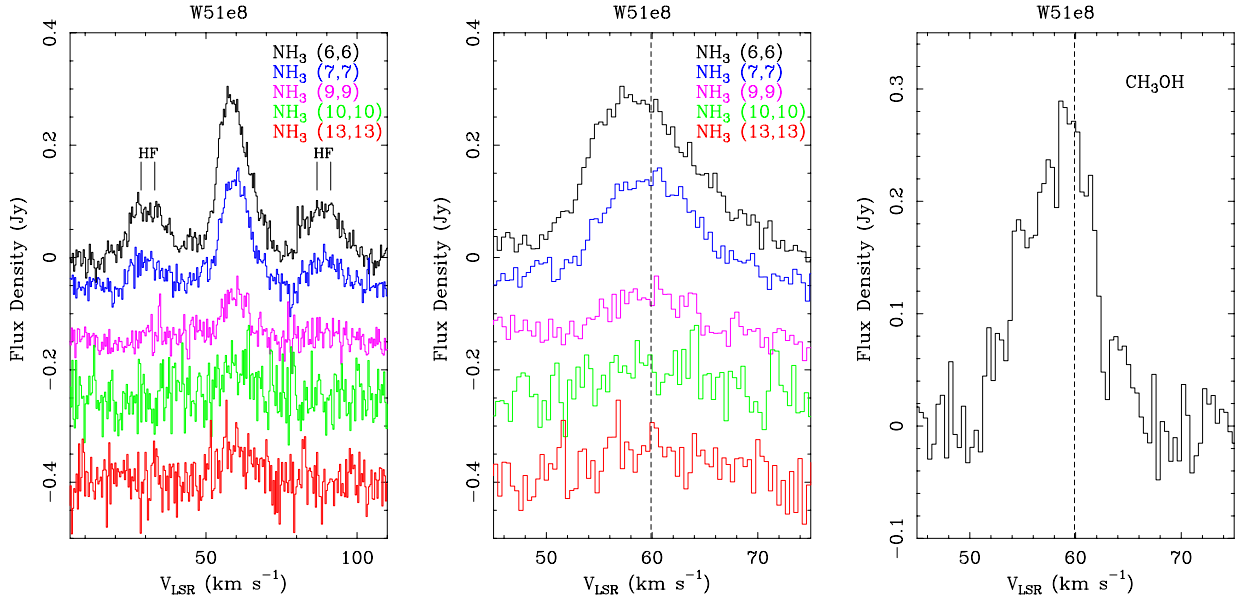


Fig. 13. Spectral profiles of emission lines arising from hot molecular gas around W51e8. *Left and central panels:* spectral profiles of NH_3 for transitions (6, 6), (7, 7), (9, 9), (10, 10), and (13, 13). An offset in flux density is applied to transitions adjacent in energy to better display individual profiles. The lower state energy levels of transitions shown here are $\sim 408\text{--}1691$ K (see Table 1). The hyperfine satellite lines, separated by $\sim \pm 24\text{--}31$ km s $^{-1}$ (see Table 3), are detected for the (6, 6), (7, 7), and (9, 9) lines (*left panel*). A narrower velocity range is plotted in the *central panel* to show the line profiles of the main hyperfine component of each inversion transition more clearly. *Right panel:* spectral profile of the $J_K = 13_2\text{--}13_1$ line of CH_3OH ($\nu_{\text{rest}} = 27.473$ GHz). The velocity resolution is 0.4 km s $^{-1}$ (*all panels*) and the vertical dashed line indicates a velocity of 59.9 km s $^{-1}$ (*central and right panels*).

outflow (~ 100 km s $^{-1}$), a slower expanding wide-angle shell (~ 10 km s $^{-1}$), and potentially an infalling envelope associated with W51e2-E. Interestingly, our hot NH_3 measurements provide supporting evidence for the latter.

Although deriving the velocity field for the emission is more problematic than for absorption (owing to lower S/N), we have four lines of evidence indicating accretion/infall of the hot thermal gas around W51e2-E. First, the spectral profiles show that the lower excitation (more optically thick) lines are double peaked; the blueshifted component is stronger than the redshifted component, while the higher excitation (more optically thin) lines are more symmetric (Sect. 3.2). This feature is a well-understood signature of infall in a centrally condensed core. In fact, in a collapsing core, the blue side and red side of the line arise from the rear and front side of the core, respectively. The redshifted portion of the emission comes mainly from the outer (and cooler) region in the front side, whereas the blueshifted portion comes from the inner (and hotter) region in the rear side. This geometrical asymmetry produces a stronger blue shoulder in line profiles relative to the red shoulder. This asymmetry decreases with the decrease of optical depth, and the line becomes symmetric when it is optically thin because radiation from different parts of the core is not absorbed. In exceptional cases, such as the strong hot-core G31.41+0.31, it has been possible to show this effect with spatially resolved maps of the intensity profiles as a function of distance to the center (e.g., [Mayen-Gijon et al. 2014](#)). In general, however, the S/N as well as the spatial resolution is too poor to attempt such an analysis, as is also the case for W51e2. Therefore, the signature of infall simply from spectral profiles remains ambiguous; we cannot exclude for example that an asymmetric spectral profile (skewed to the blue side) could arise from an outflow with a stronger blueshifted lobe. Nevertheless, a second line of evidence supporting the hypothesis of infall is provided by the pv diagram, which shows a C-shaped structure (in the blueshifted side) and, although less

clear, an O-shaped structure (when the redshifted side is also included; see Fig. 7). This feature is expected for a radially infalling core where the l.o.s. velocity displacement is expected to be maximum at the center and then to decrease away from it. In addition, the velocity field map shows some weak redshifted emission in the vicinity of W51e2-E (Fig. 6), which further supports the hypothesis of infalling gas. Finally, toward W51e2-E we estimate the highest NH_3 column density in the W51e2 complex (with the exception of the HII region), which is inconsistent with outflowing gas. We conclude that W51e2-E is a high-mass protostar, driving a powerful outflow and potentially associated with an infalling massive envelope.

W51e2-W. In the majority of previous studies, the HC HII region was thought to be the center of star formation activity in the W51e2 complex. However, recent studies exploiting increasing angular resolution, including the present study, show that this is not the case. The overlays in Figs. 14 and 16, show that there is no molecular outflow arising from the HC HII region, at least based on CO emission and/or H_2O masers. The presence of an ionized outflow has been postulated to interpret the SW extension ([Gaume et al. 1993](#)), but our new measurements do not bring in any additional evidence. The bulk of CH_3OH maser emission is concentrated onto the nearby companion W51e2-E, and only a few maser spots are observed in the western edge of the HC HII region, having blueshifted emission (Fig. 15, top panel) in agreement with the velocity structure observed in NH_3 (see Fig. 2). Several OH masers are still observed at the edges of the HII region (Fig. 15, bottom panel). Their proper motions indicate an isotropic slow expansion from the HII region with a velocity of $\lesssim 10$ km s $^{-1}$ (Fig. 17), which is consistent with the generally accepted scenario where OH masers are excited during the late stages of expanding UC HII regions (e.g., [Fish & Reid 2007](#)).

Although these findings point to a much lower degree of star formation activity with respect to the nearby W51e2-E, the

Table 2. Parameters of the NH₃ inversion lines observed around W51 Main.

Line (<i>J, K</i>)	F_{peak} (Jy)	V_c (km s ⁻¹)	$\Delta V_{1/2}$ (km s ⁻¹)	F_{int} (Jy km s ⁻¹)	F_{cont} (Jy)
W51e2-W (HC HII)					
J2000 19:23:43.9054 +014.30.34.487, 0.8'' × 0.9'', PA = 0 deg					
(6, 6)	-0.336 ± 0.001	57.14 ± 0.01	7.29 ± 0.03	-2.61 ± 0.01	0.362
(7, 7)	-0.310 ± 0.001	57.09 ± 0.01	5.93 ± 0.02	-1.96 ± 0.01	0.362
(9, 9)	-0.227 ± 0.001	57.22 ± 0.01	5.54 ± 0.03	-1.34 ± 0.01	0.346
(10, 10)	-0.150 ± 0.004	57.45 ± 0.06	4.38 ± 0.14	-0.70 ± 0.03	0.258
(13, 13)	-0.072 ± 0.004	57.53 ± 0.12	3.87 ± 0.28	-0.30 ± 0.03	0.369
CH ₃ OH	-0.287 ± 0.006	57.72 ± 0.04	4.12 ± 0.09	-1.30 ± 0.03	0.346
W51e2-E (protostar)					
J2000 19:23:43.9600 +014.30.34.500, 0.9'' × 0.9'', PA = 0 deg					
(6, 6)	0.044 ± 0.001	57.00 ± 0.12	14.5 ± 0.3	0.68 ± 0.02	–
(7, 7)	0.046 ± 0.001	56.30 ± 0.10	10.9 ± 0.2	0.53 ± 0.02	–
(9, 9)	0.023 ± 0.001	56.24 ± 0.19	11.6 ± 0.5	0.28 ± 0.02	–
(10, 10)	0.020 ± 0.003	54.81 ± 0.70	8.74 ± 1.65	0.18 ± 0.05	–
(13, 13)	0.036 ± 0.004	55.53 ± 0.27	4.63 ± 0.64	0.18 ± 0.03	–
CH ₃ OH	0.040 ± 0.003	56.48 ± 0.27	8.80 ± 0.65	0.37 ± 0.03	–
W51e2-NW (protostar)					
J2000 19:23:43.900 +014.30.35.980, 1.3'' × 2'', PA = 0 deg					
(6, 6)	0.099 ± 0.002	55.72 ± 0.08	10.7 ± 0.2	1.12 ± 0.03	–
(7, 7)	0.075 ± 0.002	55.24 ± 0.09	7.72 ± 0.22	0.62 ± 0.02	–
(9, 9)	0.028 ± 0.002	55.64 ± 0.30	7.36 ± 0.70	0.22 ± 0.03	–
(10, 10)	–	–	–	–	–
(13, 13)	–	–	–	–	–
CH ₃ OH	0.084 ± 0.004	55.46 ± 0.16	6.8 ± 0.4	0.61 ± 0.03	–
W51e2-E+NW (entire core)					
(6, 6)	0.432 ± 0.003	55.38 ± 0.04	10.7 ± 0.2	4.90 ± 0.06	–
(7, 7)	0.310 ± 0.004	55.53 ± 0.05	8.57 ± 0.1	2.82 ± 0.05	–
(9, 9)	0.099 ± 0.004	55.90 ± 0.20	8.98 ± 0.5	0.94 ± 0.07	–
(10, 10)	0.059 ± 0.007	54.32 ± 0.8	13.0 ± 2	0.82 ± 0.16	–
(13, 13)	0.069 ± 0.012	55.77 ± 0.43	5.1 ± 1.0	0.38 ± 0.10	–
CH ₃ OH	0.444 ± 0.010	55.6 ± 0.1	8.3 ± 0.2	3.92 ± 0.09	–
W51e8					
J2000 19:23:43.9076 +014.30.28.068, 3.1'' × 4.3'', PA = 0 deg					
(6, 6)	0.279 ± 0.003	59.06 ± 0.07	12.39 ± 0.17	3.67 ± 0.07	–
(7, 7)	0.190 ± 0.004	59.73 ± 0.11	11.20 ± 0.26	2.27 ± 0.07	–
(9, 9)	0.083 ± 0.005	59.65 ± 0.31	11.20 ± 0.73	0.99 ± 0.09	–
(10, 10)	0.059 ± 0.009	60.60 ± 0.92	12.36 ± 2.17	0.78 ± 0.18	–
(13, 13)	0.063 ± 0.012	59.82 ± 1.24	13.28 ± 2.93	0.88 ± 0.26	–
CH ₃ OH	0.260 ± 0.009	58.43 ± 0.14	7.82 ± 0.32	2.16 ± 0.08	–

Notes. The peak fluxes (F_{peak} , Col. 2), the central velocities (V_c ; Col. 3), the FWHM line width ($\Delta V_{1/2}$; Col. 4), and the velocity-integrated flux (F_{int} ; Col. 5) are estimated from single-Gaussian fits to the spectral profiles of the main lines. The table also reports the continuum emission flux density at the corresponding frequency of the inversion lines seen in absorption (F_{cont} ; Col. 6).

absorption spectrum of the NH₃ inversion lines (detected up to the most excited levels) indicates the presence of a hot core still surrounding the HC HII region. We estimate an upper limit of about 5 M_{\odot} of molecular material (assuming $[\text{NH}_3]/[\text{H}_2] = 10^{-7}$) still present in the immediate environs of the HC HII region (within 0'.06, 320 AU). This material could be potentially accreting onto the central YSO, either in the form of an accretion disk or an infalling envelope, provided that it has not been stopped by the intense radiation pressure from the central O-type star and the thermal pressure from the ionized gas in the HII region. Indeed, the observed velocity gradient provides

evidence for rotation in the molecular core surrounding the HC HII (Sect. 3.1.1).

Zhang & Ho (1997) noticed an increase of the gradient seen in the NH₃ (3,3) line moving inward in radius (with a slope $r^{-1.2}$), and suggested that the rotating material was spinning up during collapse. We do not spatially resolve the gradient and therefore we cannot measure the rotation curve. Nevertheless, our NH₃ velocity field maps do not show a clear steepening of the gradient with increasing excitation energy. If the molecular gas were in differential (e.g., Keplerian) rotation, one would expect warmer gas closer to the central YSO to move faster. We

Table 3. Parameters of the hyperfine components of NH₃ inversion lines observed around W51 Main.

Line (<i>J</i> , <i>K</i>)	$\Delta\nu_{HF}$ (MHz)		ΔV_{HF} (km s ⁻¹)		a_{ms}	F_{peak} (Jy)	$\Delta V_{1/2}$ (km/s)	F_{int} (Jy km/s)	V_c (km/s)	Peak opacity (τ)
	Inner	Outer	Inner	Outer						
W51e2-W (HC HII)										
(6, 6)	± 2.24	± 2.62	± 26.9	± 31.4	0.0081	-0.162 ± 0.001	4.29 ± 0.04	-0.74 ± 0.01	57.55 ± 0.01	81 ± 9
(7, 7)	± 2.34	± 2.68	± 27.3	± 31.2	0.0060	-0.0642 ± 0.0009	4.52 ± 0.12	-0.31 ± 0.01	57.22 ± 0.03	39 ± 8
(9, 9)	± 2.48	± 2.75	± 27.0	± 30.1	0.0037	-0.0097 ± 0.0003	3.60 ± 0.20^a	-0.067 ± 0.003	57.36 ± 0.16	12 ± 9
W51e2-E (protostar)										
(6, 6)	± 2.24	± 2.62	± 26.9	± 31.4	0.0081	0.0225 ± 0.0003	9.02 ± 0.12	0.217 ± 0.004	56.40 ± 0.09	89 ± 86
(7, 7)	± 2.34	± 2.68	± 27.3	± 31.2	0.0060	0.0104 ± 0.0002	9.56 ± 0.24	0.106 ± 0.003	56.39 ± 0.18	43 ± 59
(9, 9)	± 2.48	± 2.75	± 27.0	± 30.1	0.0037	0.0034 ± 0.0002	6.93 ± 0.59	0.025 ± 0.003	56.47 ± 0.43	43 ± 124
W51e2-NW (protostar)										
(6, 6)	± 2.24	± 2.62	± 26.9	± 31.4	0.0081	0.0150 ± 0.0005	8.54 ± 0.32	0.136 ± 0.007	55.27 ± 0.22	20 ± 15
(7, 7)	± 2.34	± 2.68	± 27.3	± 31.2	0.0060	0.0043 ± 0.0004	8.83 ± 1.03	0.040 ± 0.006	54.13 ± 0.76	10 ± 16
(9, 9)	± 2.48	± 2.75	± 27.0	± 30.1	0.0037	–	–	–	–	–
W51e2-E+NW (entire core)										
(6, 6)	± 2.24	± 2.62	± 26.9	± 31.4	0.0081	0.0675 ± 0.0009	9.6 ± 0.16	0.692 ± 0.014	55.28 ± 0.11	21 ± 2
(7, 7)	± 2.34	± 2.68	± 27.3	± 31.2	0.0060	0.0186 ± 0.0008	9.1 ± 0.5	0.180 ± 0.012	56.39 ± 0.35	10 ± 16
(9, 9)	± 2.48	± 2.75	± 27.0	± 30.1	0.0037	–	–	–	–	–
W51e8										
(6, 6)	± 2.24	± 2.62	± 26.9	± 31.4	0.0081	0.0469 ± 0.0004	14.1 ± 0.4	0.705 ± 0.007	59.85 ± 0.18	23 ± 3
(7, 7)	± 2.34	± 2.68	± 27.3	± 31.2	0.0060	0.0267 ± 0.0009	9.2 ± 0.4	0.260 ± 0.01	60.03 ± 0.30	25 ± 3
(9, 9)	± 2.48	± 2.75	± 27.0	± 30.1	0.0037	0.0083 ± 0.0006	14.1 ± 0.4	0.129 ± 0.009	63.5 ± 1.3	28 ± 6

Notes. Frequency separations ($\Delta\nu_{HF}$, Cols. 2 and 3) of the four satellite components were calculated using Eq. (B.1). The corresponding velocity separations (ΔV_{HF}) are also reported in Cols. 4 and 5. a_{ms} (Col. 6) is the theoretical ratio of the satellite line to the main line strengths calculated using Eqs. (B.2). F_{peak} , F_{int} , and $\Delta V_{1/2}$ were fitted simultaneously for all the hyperfine quadrupole satellite components assuming a Gaussian shape for each of the hyperfine lines. The values reported in the table are average values of the four Gaussians fitted to the HFS satellites. τ (Col. 11) is the line opacity estimated numerically with Eq. (A.1) from Paper I.

^(a) The best-fit parameters for the (9, 9) line come from a fit that allowed the velocity offset of the two hyperfine lines to vary, since for the (9, 9) line only, the fixed-offset hyperfine fit was of poor quality.

Table 4. High-mass YSOs hosting hot cores in W51 Main.

Source name	RA (J2000) (h:m:s)	Dec (J2000) (°:′:″)	V_{LSR} (km s ⁻¹)	T_{rot}^a (K)	N (cm ⁻³)	R_{core}^b (AU)	M_{gas}^c (M_{\odot})	Outflow (Y/N)	Disk (Y/N)
W51e2-W	19:23:43.9096	14:30:34.551	57.4	174	6.9×10^{13}	320	5	N	Y
W51e2-E	19:23:43.9618	14:30:34.558	56.4	173	5.1×10^7	2430	18	Y	N
W51e2-NW	19:23:43.8900	14:30:35.630	55.2	144	1.6×10^7	4460	32	Y	N
W51e8	19:23:43.9073	14:30:28.197	59.9	204	2.7×10^6	10200	69	Y	N

Notes. ^(a) In the case of emission lines, rotational temperatures are calculated in the optically thin assumption, therefore, the quoted values are lower limits to true kinetic temperature of the gas. ^(b) The radius is defined by the area where we integrated the spectra (see Table 2 and Sect. 3.2) except for W51e2-W, for which we used the deconvolved size of the compact continuum emission quoted by Shi et al. (2010a). ^(c) The gas mass is calculated in a sphere of radius R_{core} for a given volume density ρ . For the emission, with poor estimates of the opacity, this is calculated in the optically thin assumption. Therefore, the quoted values are lower limits to the gas mass. The mass for absorption should instead be regarded as an upper limit (since we do not know the actual size of the HC HII region). These mass estimates assume $[NH_3]/[H_2] = 10^{-7}$.

cannot exclude however that this effect is hidden by optical depth effects and/or insufficient angular resolution.

Finally, since the absorption profiles appear quite symmetric and do not display a redshifted component, we do not see evidence for infall in the HII region. Gravitational collapse of the W51e2 core was suggested based on lower resolution images of lower excitation transitions of NH₃ (Zhang & Ho 1997) and other high-density tracers like CS (Zhang et al. 1998). The key evidence supporting infall was provided by both inverse P-Cygni spectral profiles (with blueshifted emission and redshifted absorption) and a C-shaped emission in pv diagrams. Since these previous studies were conducted at $\geq 1''$ resolution, both effects

could be the consequence not of infall but of insufficient angular resolution, resulting in spatial blending of (redshifted) absorption and (blueshifted) emission from the two distinct YSOs, separated by less than 1 arcsec: W51e2-W, which has a more redshifted velocity, and W51e2-E, which has a more blueshifted velocity. Additionally, the molecular absorption has a central velocity consistent with the Hn α radio RLs (Keto & Klaassen 2008; Ginsburg et al. 2016), which is not offset as would be expected if the molecular gas were infalling¹¹. We conclude that

¹¹ Even in the assumption of infall of the ionized gas, we would still expect the (optically thin) RLs to be at the systemic velocity.

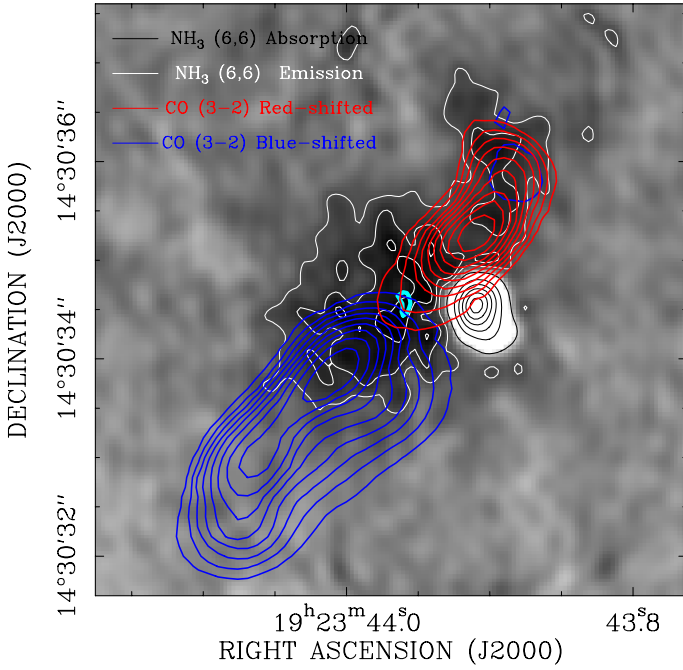


Fig. 14. Overlay of the CO $J = 3-2$ 0th moment image from the SMA (blue and red contours; Shi et al. 2010b) onto the total intensity (0th moment) map of the (6,6) inversion transition of NH_3 (gray scale and white+black contours). The NH_3 emission is shown with white contours, representing 30% to 90% with steps of 20% of the line peak for the (6,6) line, $107 \text{ mJy beam}^{-1} \text{ km s}^{-1}$. The NH_3 absorption is shown with black contours, representing factors 1, 5, 9,.... of $-50 \text{ mJy beam}^{-1}$, for all transitions. The CO 3-2 line contours are from 10% to 90% with steps of 10% of the line peak ($67 \text{ Jy beam}^{-1} \text{ km s}^{-1}$ for the red contours and $82 \text{ Jy beam}^{-1} \text{ km s}^{-1}$ for the blue contours). Blue and red contours correspond to blueshifted and redshifted gas, with integrated velocity ranging from -124 to -12 km s^{-1} and from $+10$ to $+116 \text{ km s}^{-1}$, respectively. The cyan contour locates the peak of the total intensity map of the most highly excited NH_3 transitions (13, 13); we assume that this peak pinpoints the high-mass YSO driving the CO outflow.

based on our new NH_3 measurements, the evidence of infall toward the W51e2-W HII region is lacking.

W51e2-NW. W51e2-NW is a massive core first detected in dust emission $1''$ north of W51e2-W, and could be an additional YSO in the W51e2 clump (Shi et al. 2010a). Since no continuum emission has been detected at $\lambda \geq 7 \text{ mm}$, this YSO could be at an earlier phase of star formation. Since we detect hot NH_3 up to the (9,9) doublet, W51e2-NW must be also exciting a hot molecular core. We estimate $32 M_{\odot}$ for its mass (assuming $[\text{NH}_3]/[\text{H}_2] = 10^{-7}$), which is consistent with the estimate from dust emission ($40 M_{\odot}$; Shi et al. 2010a). Given its location in the path of the molecular outflow, however, we cannot conclusively establish if W51e2-NW is an independent protostar or just a component of the same outflow driven by W51e2-E. The presence of a compact outflow, which arises from the center of the W51e2-NW core (Fig. 16, bottom panel), identified by Sato et al. (2010) using H_2O maser proper motions, supports the protostellar scenario. This H_2O maser outflow has lower velocity ($V_{\text{exp}} \sim 20 \text{ km s}^{-1}$) than the outflow driven by W51e2-E ($V_{\text{exp}} \sim 100 \text{ km s}^{-1}$) and it is elongated N-S, which is consistent with the distribution of the hot ammonia total intensity (Fig. 16, bottom panel). The simultaneous presence of hot dust and molecular gas, along with a bipolar molecular outflow, provides evidence that W51e2-NW is indeed an additional (high-mass) YSO forming in the same W51e2 core.

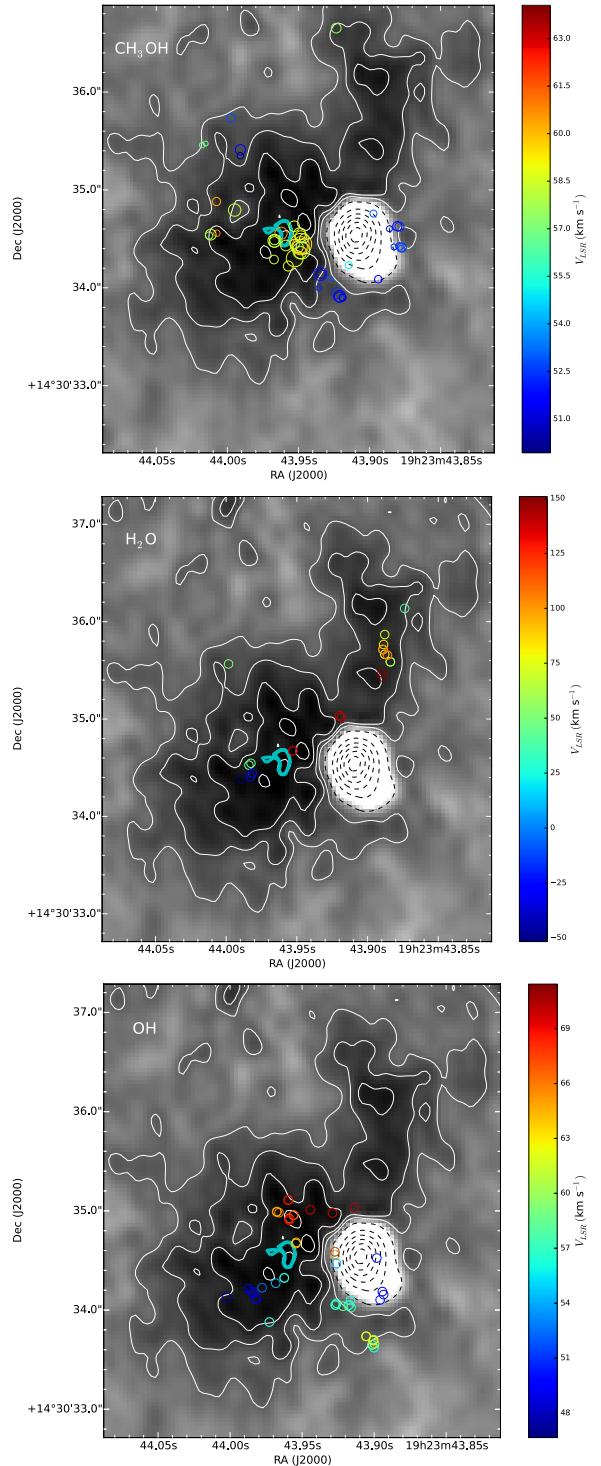


Fig. 15. Overlay of molecular masers detected around W51e2 onto the total intensity (0th moment) map of the (6,6) inversion transition of NH_3 (gray scale and white+black contours). The circles show positions of CH_3OH masers detected with MeRLIN (Etoka et al. 2012, top panel), H_2O masers detected with the VLBA (Sato et al. 2010, middle panel), and OH masers detected with the VLBA (Fish & Reid 2007, bottom panel), respectively. Colors denote l.o.s. velocity in km s^{-1} (color scale on the right-hand side in each panel). The NH_3 emission is shown with white contours, representing 20% to 100% with steps of 20% of the line peak for the (6,6) line, $107 \text{ mJy beam}^{-1} \text{ km s}^{-1}$. The NH_3 absorption is shown with black contours, representing factors 1, 5, 9,.... of $-50 \text{ mJy beam}^{-1}$. The cyan contour locates the peak of the total intensity map of the most highly excited NH_3 transitions (13, 13); the bulk of CH_3OH maser emission concentrates around the same peak. We assume that its position pinpoints the high-mass YSO W51e2-E.

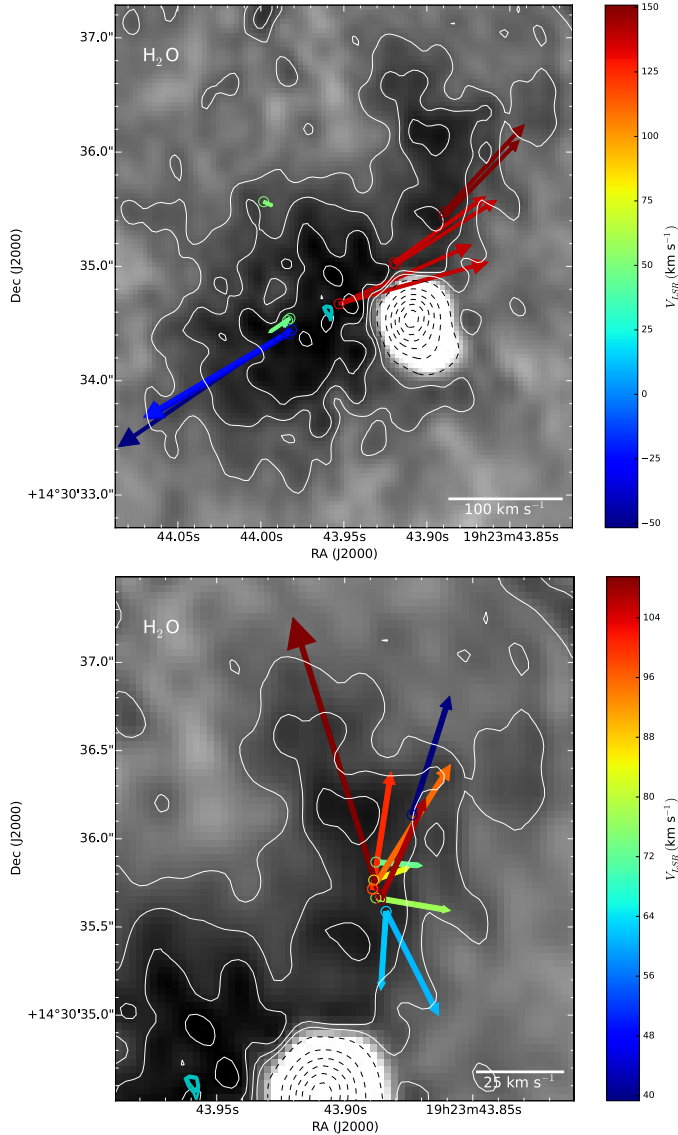


Fig. 16. Outflows identified by H_2O proper motions toward the YSOs W51e2-E (*top panel*) and W51e2-NW (*bottom panel*) (Sato et al. 2010). The position (circles) and proper motions (arrows) of water masers are overlaid onto the total intensity (0th moment) map of the (6, 6) inversion transition of NH_3 (same as Fig. 15). Colors denote l.o.s. velocity (color scale on the right-hand side in each panel) and the scale for the proper motion amplitude is given in the bottom right corner of each panel (both in km s^{-1}). The diverging proper motions identify the origin of the fast outflows, i.e., the protostellar position. The peak of the total intensity map of the most highly excited NH_3 transitions (13, 13) (cyan contours) lies at the origin of the H_2O maser outflow; we assume that its position pinpoints the high-mass YSOs W51e2-E.

5.2. W51e8

Our NH_3 measurements demonstrate that W51e8 is a massive hot core ($T \sim 200$ K, $M \sim 70 M_\odot$)¹². Zhang & Ho (1997) detected W51e8 at 22 GHz but not at 8.4 GHz, and speculated that the continuum flux is dominated by dust emission heated from a high-mass YSO. We detected a two-component structure in the 25 GHz continuum emission (e.g., see Fig. 1) and measured a declining flux density for the stronger northern component from

¹² The value quoted for the temperature is a lower limit and that for the mass assumes $[\text{NH}_3]/[\text{H}_2] = 10^{-7}$.

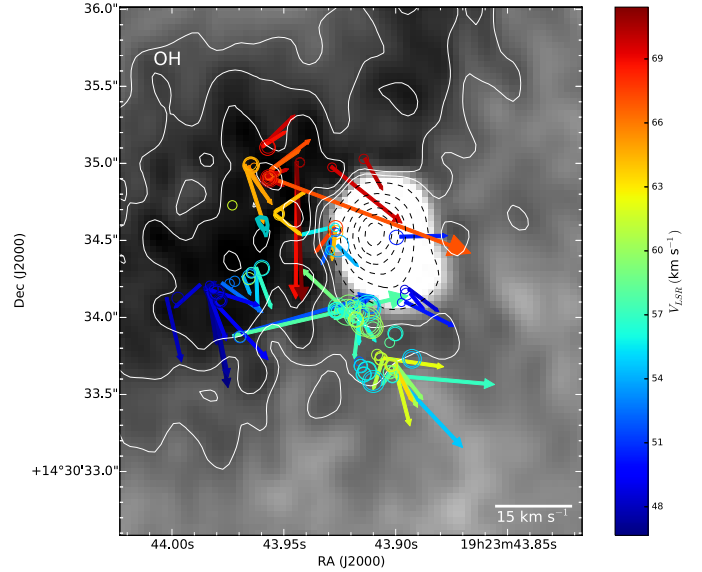


Fig. 17. OH maser proper motions measured with the VLBA toward W51e2-E (Fish & Reid 2007). The position (circles) and proper motions (arrows) of OH masers are overlaid onto the total intensity (0th moment) map of the (6, 6) inversion transition of NH_3 (same as Fig. 15). Colors denote l.o.s. velocity (color scale on the right-hand side) and the scale for the proper motion amplitude is given in the bottom right corner (both in km s^{-1}). The proper motions seem to trace a slow wide-angle expansion around W51e2-E as well as a filamentary structure south of the HC HII region.

25 GHz to 36 GHz, which is inconsistent with emission by dust; the southern component is not detected above 27 GHz. Ginsburg et al. (2016) conducted a sensitive continuum study of the W51 complex from 3.5 to 22.5 GHz, and measured spectral indices for both components of the radio continuum in W51e8, showing that it is due to free-free emission.

Figure 18 shows the OH and H_2O masers detected with the VLBA around W51e8 overlaid onto the total intensity map of the (6, 6) inversion transition. Ammonia shows a central stronger component that is elongated E-W, which is consistent with the H_2O maser spatial distribution and a more diffuse, nearly-spherical core containing the central component that is surrounded by an OH maser shell. The overlay in the top panel shows proper motions of OH masers, which are globally suggestive of isotropic expansion of a molecular shell around W51e8 (Fish & Reid 2007). A closer inspection reveals that expansion is the dominant motion in the maser clusters to the NW and NE, while masers in other locations show more complex proper motion patterns, including inflow. On the other hand, the bottom panel shows that H_2O masers identify a bipolar outflow along approximately the E-W direction and with an expansion velocity of about 20 km s^{-1} (Sato et al. 2010). The overlays show also that the 25 GHz radio continuum peak and the total intensity of the (13, 13) NH_3 line, are spatially coincident and fall at the center of the OH maser shell and the H_2O maser bipolar outflow. We assume that this position locates the exciting high-mass YSO (this is the position reported in Table 4).

What about the velocity field of the NH_3 gas? As in the case of W51e2-E, the NH_3 emission lines show asymmetric spectral profiles, which may in principle indicate inflow; the lower excitation (more optically thick) lines are double peaked, and the blueshifted component is stronger than the redshifted component, while the higher excitation (more optically thin lines) are

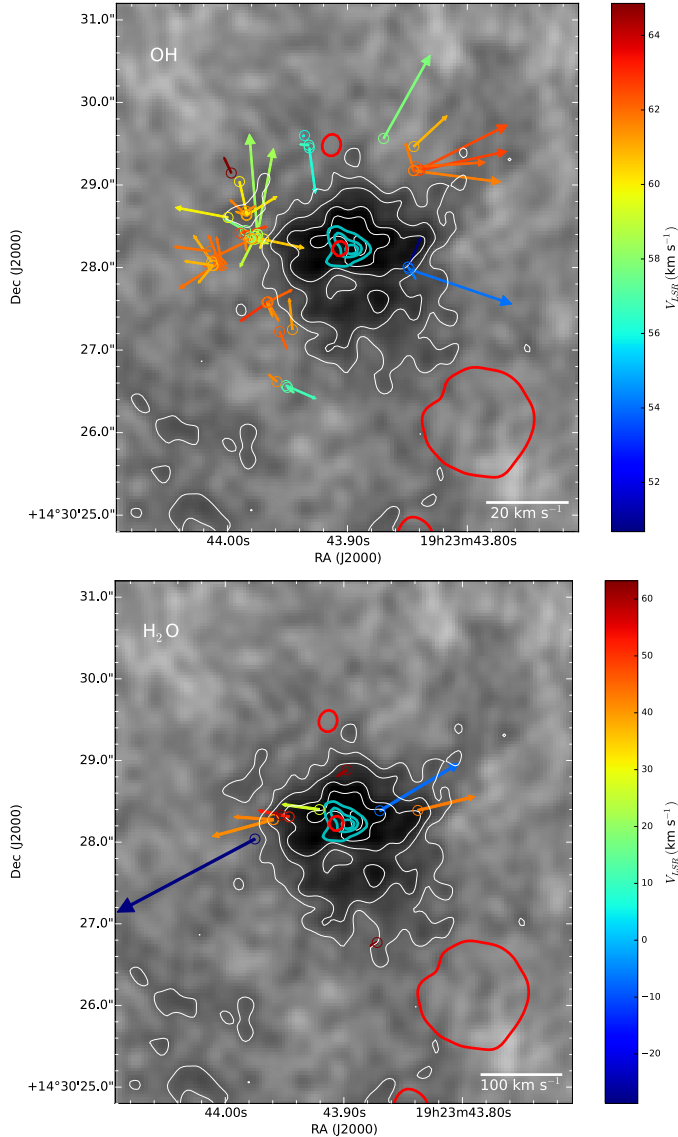


Fig. 18. Overlay of molecular masers detected around W51e8 onto the total intensity (0th moment) map of the (6,6) inversion transition of NH_3 (gray scale and white+black contours). The circles show positions and the arrows indicate proper motions of OH masers (Fish & Reid 2007) (top panel), and H_2O masers (Sato et al. 2010) (bottom panel), respectively, both measured with the VLBA. Colors denote l.o.s. velocity (color scale on the right-hand side in each panel) and the scale for the proper motion amplitude is given in the bottom right corner of each panel (both in km s^{-1}). The NH_3 emission is shown with white contours, representing 20% to 100% with steps of 20% of the line peak for the (6,6) line, $107 \text{ mJy beam}^{-1} \text{ km s}^{-1}$. The red contour indicates the 3 mJy flux level per beam (corresponding to $\sim 4\sigma$ where $\sigma \sim 0.7 \text{ mJy beam}^{-1}$) for the 25 GHz continuum emission. Besides W51e1 to the SW, a peak of the radio continuum falls at the peak of the total intensity map of the most highly excited NH_3 transitions (13, 13), which are indicated with cyan contours. We assume that its position pinpoints a high-mass YSO at the center of W51e8, driving both a fast H_2O maser outflow and a more slowly expanding OH maser shell.

more symmetric. Zhang et al. (1998) claimed infall of the molecular core (infall speed of 3.5 km s^{-1}) based on line asymmetries in CS and CH_3CN . However, in the case of W51e8 we do not have supporting evidence of infall from the spatially resolved maps of the velocity field so the infall signature from spectral

profiles remains ambiguous. In fact, alternative explanations are possible. For example, Fig. 6 shows predominantly redshifted emission toward the east and blueshifted emission toward the west, which may be related to the outflow. Consistently, a pv diagram at $\text{PA} = 90$ shows a velocity gradient in the central component (Fig. 10, top panel). A pv diagram in the perpendicular direction also shows a hint of velocity gradient, which may indicate rotation in the direction perpendicular to the outflow, although the signature is less clear than along the outflow axis (Fig. 10, bottom panel). The H_2O masers show that the fastest components of the outflow have blueshifted velocities (Fig. 18, bottom panel). Therefore, the asymmetric spectral profiles (skewed to the blue side) could be due to an outflow with a stronger blueshifted lobe. We conclude that the core surrounding W51e8 may be not contracting after all.

6. Summary

We imaged the W51 Main complex with the JVLA at ~ 0.2 resolution in five metastable inversion transitions of ammonia, which are emitted from doublet levels from about 400 K up to 1700 K above the ground state. We also imaged the radio continuum emission from 25 GHz to 36 GHz in the region. Our NH_3 maps reveal the presence of four individual hot cores in W51-Main, presumably hosting high-mass YSOs at their centers, which seem to be in different evolutionary stages: W51e2-W, W51e2-E, W51e2-NW, and W51e8. Our NH_3 (and continuum) measurements, along with previously published data, enabled us to derive physical and dynamical properties of the identified YSOs, which we describe in detail below.

1. The HC III region W51e2-W has been generally considered the center of star formation activity in the W51 Main complex. The flux of Lyman continuum photons inferred from radio recombination lines and the radio continuum flux require an O8-type YSO as an exciting source to maintain ionisation (Shi et al. 2010a; Ginsburg et al. 2016). Despite the fact that the exciting YSO has already reached the ZAMS, our NH_3 maps identify a hot molecular core ($T_{\text{gas}} \sim 170 \text{ K}$) surrounding the HC III region. The core has a clear velocity gradient ($\Delta V \sim 4.4 \text{ km s}^{-1}$), which we interpret as rotation in the E-W direction. While this finding may suggest the presence of a rotating disk and that mass accretion maybe be still ongoing, the velocity field maps of NH_3 lines at different excitation energy do not show a clear velocity gradient increase toward the interior as would be expected if material was spinning up during accretion. Likewise, we do not discern a Keplerian velocity profile (at spatial resolution of order of 1000 AU). Higher resolution data of optically thin lines from the same molecular species may be required to confirm both effects. While the lower limit to the mass of the central YSO is $20 M_{\odot}$, we estimate a total molecular gas mass of only $5 M_{\odot}$ from the NH_3 lines (assuming $X_{\text{NH}_3} = 10^{-7}$), suggesting that most of the mass has been already accreted onto the central star. The lack of outflow and/or $\text{H}_2\text{O}/\text{CH}_3\text{OH}$ maser activity supports the idea that the main accretion phase may be (nearly) over for this O-type YSO.
2. W51e2-E (0.8 eastward from the HC III region) possesses the typical features of an embedded high-mass protostar at an early stage of HMSF: bright continuum dust emission but lack of free-free or RL emission, hot core activity ($T_{\text{gas}} \sim 170 \text{ K}$ from NH_3), strong CH_3OH masers, powerful molecular outflow, organized magnetic field structure (Tang et al. 2009; Zhang et al. 2014). While we do not find clear

indication of rotation in the circumstellar gas surrounding W51e2-E, there are some indications of collapse/infall. In fact, the NH_3 line profiles from lower excitation (i.e., thicker) lines show suppressed redshifted emission as compared with the blueshifted emission component, while the line asymmetry disappears in higher excitation (i.e., thinner) lines. This is a well-understood signature of infall in a dense core. Supporting evidence is also provided by an O-shaped pv diagram and redshifted emission in the vicinity of W51e2-E. The indication of infalling gas, coupled with powerful outflow and maser activity suggests that the center of accretion in the W51e2 complex is the embedded W51e2-E protostar rather than the neighboring HC HII region. We do not know the actual mass of the protostar, but we estimate about $20 M_\odot$ worth of molecular material (assuming $[\text{NH}_3]/[\text{H}_2] = 10^{-7}$) within half an arcsecond or about 2500 AU from the putative protostellar position (Shi et al. 2010a estimated $140 M_\odot$ for the total core mass). This indicates that the natal core has enough material available for accretion onto the central protostar to become an O-type star.

3. W51e2-NW is an additional hot molecular core ($T_{\text{gas}} \sim 140$ K from NH_3) in the W51e2 complex ($1''$ north of the HC HII region), initially detected in dust emission and now in hot NH_3 up to the (9, 9) doublet. We estimate $32 M_\odot$ of molecular gas for this hot core (assuming $[\text{NH}_3]/[\text{H}_2] = 10^{-7}$). W51e2-NW does not exhibit continuum emission at $\lambda > 7$ mm nor $\text{CH}_3\text{OH}/\text{OH}$ masers (Etoka et al. 2012; Fish & Reid 2007), but it drives an H_2O maser outflow; this may indicate a protostellar core, either at an earlier evolutionary stage or with a lower mass than W51e2-E.
4. W51e8 contains a large amount ($\sim 70 M_\odot$, assuming $[\text{NH}_3]/[\text{H}_2] = 10^{-7}$) of warm ($T \sim 200$ K) molecular gas, as derived from our NH_3 measurements. It drives a bipolar outflow (traced by H_2O masers) indicating the presence of a high-mass protostar at its center, whose position is pinpointed by the peaks in both the (13, 13) NH_3 total intensity and the 25 GHz radio continuum emissions. The latter can be interpreted in terms of an ionized jet, pointing to a hot core stage prior to the onset of a HC HII region. The presence of an OH maser shell slowly expanding ($\sim 10 \text{ km s}^{-1}$) around the NH_3 core is however inconsistent with this hypothesis, since OH maser shells are a typical signpost of expanding UC HII regions. Likewise, the lack of methanol maser emission, which is a typical signpost of HMSF, is puzzling; this deficiency could be explained with the low molecular density estimated for the e8 core, $\sim 10^6 \text{ cm}^{-3}$, which is insufficient to efficiently pump CH_3OH masers (which require $N_{\text{H}_2} \geq 10^7 \text{ cm}^{-3}$; Cragg et al. 2005). Moreover, it is not clear what is the dominant motion in the hot molecular gas (although expansion is more probable). Further observations are needed to clarify the evolutionary stage and gas kinematics of W51e8 within W51 Main.

This study of W51 Main demonstrates that high-angular resolution imaging (with a few tenths of arcseconds) of high-excitation lines of NH_3 at ~ 1 cm wavelengths are well suited to study the kinematics and physical conditions of the hottest and densest molecular gas in HMSF complexes where O-type stars are forming. W51 Main offers the rare opportunity to compare physical and dynamical properties of high-mass YSOs at different evolutionary stages forming in the same clump.

Acknowledgements. We thank the anonymous referee for a thorough effort in reviewing the manuscript and a very constructive report. We are grateful to Dr. Vincent Fish for providing the OH proper motion measurements. We are grateful to Riccardo Cesaroni for useful discussions. These data were obtained under JVLA program 12A-274. Spectral line fitting was performed using the pyspeckit package (Ginsburg & Mirocha 2011).

References

- Arce, H. G., Shepherd, D., Gueth, F., et al. 2007, *Protostars and Planets V*, 951, 245
- Cragg, D. M., Sobolev, A. M., & Godfrey, P. D. 2005, *MNRAS*, 360, 533
- Etoka, S., Gray, M. D., & Fuller, G. A. 2012, *MNRAS*, 423, 647
- Fish, V. L., & Reid, M. J. 2007, *ApJ*, 670, 1159
- Gaume, R. A., Johnston, K. J., & Wilson, T. L. 1993, *ApJ*, 417, 645
- Ginsburg, A., & Mirocha, J. 2011, Astrophysics Source Code Library [record ascl:1109.001]
- Ginsburg, A., Goss, W. M., Goddi, C., et al. 2016, *A&A*, submitted
- Goddi, C., Zhang, Q., & Moscadelli, L. 2015a, *A&A*, 573, A108
- Goddi, C., Henkel, C., Zhang, Q., Zapata, L., & Wilson, T. L. 2015b, *A&A*, 573, A109
- Hernández-Hernández, V., Zapata, L., Kurtz, S., & Garay, G. 2014, *ApJ*, 786, 38
- Ho, P. 1972, Ph.D. Thesis, MIT, MA, USA
- Ho, P. T. P., & Townes, C. H. 1983, *ARA&A*, 21, 239
- Imai, H., Watanabe, T., Omodaka, T., et al. 2002, *PASJ*, 54, 741
- Keto, E., & Klaassen, P. 2008, *ApJ*, 678, L109
- Mangum, J. G., & Shirley, Y. L. 2015, *PASP*, 127, 266
- Mauersberger, R., Henkel, C., Wilson, T. L., & Walmsley, C. M. 1986, *A&A*, 162, 199
- Mayen-Gijon, J. M., Anglada, G., Osorio, M., et al. 2014, *MNRAS*, 437, 3766
- Mehring, D. M. 1994, *ApJS*, 91, 713
- Osorio, M., Anglada, G., Lizano, S., & D'Alessio, P. 2009, *ApJ*, 694, 29
- Pickett, H. M., Poynter, R. L., Cohen, E. A., et al. 1998, *J. Quant. Spectr. Rad. Transf.*, 60, 883
- Remijan, A., Sutton, E. C., Snyder, L. E., et al. 2004, *ApJ*, 606, 917
- Sato, M., Reid, M. J., Brunthaler, A., & Menten, K. M. 2010, *ApJ*, 720, 1055
- Shi, H., Zhao, J.-H., & Han, J. L. 2010a, *ApJ*, 710, 843
- Shi, H., Zhao, J.-H., & Han, J. L. 2010b, *ApJ*, 718, L181
- Sollins, P. K., & Ho, P. T. P. 2005, *ApJ*, 630, 987
- Surcis, G., Vlemmings, W. H. T., van Langevelde, H. J., & Hutawarakorn, B. 2012, *A&A*, 541, A47
- Tang, Y.-W., Ho, P. T. P., Koch, P. M., et al. 2009, *ApJ*, 700, 251
- Townes, C. H., & Schawlow, A. L. 1975, *Astrophys. Lett.*, 16, 184
- Wilson, T. L., Rohlfs, K., & Hüttemeister, S. 2009, *Tools of Radio Astronomy* (Springer-Verlag)
- Xu, Y., Reid, M. J., Menten, K. M., et al. 2009, *ApJ*, 693, 413
- Zhang, Q., & Ho, P. T. P. 1995, *ApJ*, 450, L63
- Zhang, Q., & Ho, P. T. P. 1997, *ApJ*, 488, 241
- Zhang, Q., Ho, P. T. P., & Ohashi, N. 1998, *ApJ*, 494, 636
- Zhang, Q., Qiu, K., Girart, J. M., et al. 2014, *ApJ*, 792, 116

Appendix A: Methods to estimate the physical conditions of the NH₃ gas

A.1. Absorption

We follow the approach for determining column density in a given rotational state from [Mangum & Shirley \(2015\)](#). For each transition, we compute the column density of molecules in the lower transition state (N_l) starting with Eq. (30) in [Mangum & Shirley \(2015\)](#):

$$N_l = \frac{3h}{8\pi^3|\mu_{ul}|^2} \left[\exp\left(\frac{h\nu}{kT}\right) - 1 \right]^{-1} \int \tau_\nu d\nu.$$

Using:

$$|\mu_{jk}|^2 \equiv S\mu^2$$

$$S = \frac{K^2}{J(J+1)} \text{ (for } (J, K) \rightarrow (J, K) \text{ transitions),}$$

we find that the metastable states of NH₃ ($N_u = N(J, K)$) can be described by

$$N(J, K) = \frac{3h}{8\pi^3|\mu|^2} \frac{J(J+1)}{K^2} \left[\exp\left(\frac{h\nu}{kT}\right) - 1 \right]^{-1} \int \tau_\nu d\nu. \quad (\text{A.1})$$

If we further assume that the Rayleigh-Jeans approximation applies ($h\nu \ll kT$),

$$\exp\left(\frac{h\nu}{kT}\right) - 1 = \frac{h\nu}{kT},$$

we obtain the following:

$$\begin{aligned} N(J, K) &= \frac{3h}{8\pi^3|\mu|^2} \frac{J(J+1)}{K^2} \frac{kT_{\text{ex}}}{h\nu} \int \tau_\nu d\nu \\ &= \frac{3k}{8\pi^3|\mu|^2} \frac{J(J+1)}{K^2} \frac{T_{\text{ex}}}{\nu} \int \tau_\nu d\nu. \end{aligned} \quad (\text{A.2})$$

For NH₃, $\mu = 1.468 \times 10^{18}$ esu cm. Inserting this value for μ and the other physical constants results in the following:

$$N(J, K) = 7.7 \times 10^{13} \frac{J(J+1)}{K^2} \frac{T_{\text{ex}}}{\nu} \int \tau_\nu d\nu. \quad (\text{A.3})$$

We use peak optical depth and FWHM line widths to approximate the integration over the line profile, therefore Eq. (A.7) in [Mangum & Shirley \(2015\)](#) applies, implying that a factor of 0.94 should be included in the prefactor of the equation for $N(J, K)$ above, resulting in

$$N(J, K) = 7.3 \times 10^{13} \frac{J(J+1)}{K^2} \frac{\Delta\nu}{\nu} \tau T_{\text{ex}}, \quad (\text{A.4})$$

where $N(J, K)$ is in cm⁻², $\Delta\nu$ is the line width (in km s⁻¹), ν is the transition frequency (in GHz), T_{ex} is the excitation temperature (in K), and τ is the line opacity (derived numerically solving Eq. (A.1) from Paper I).

In order to find the total column density, we assume that all the energy levels are populated according to a Boltzmann distribution, characterized by a single T_{rot} ,

$$N_{\text{tot}} = \frac{N(J, K)}{g(J, K)} Q(T_{\text{rot}}) e^{E_l/T_{\text{rot}}}, \quad (\text{A.5})$$

where $g(J, K) = g_{\text{op}}(2J+1)$ are the statistical weights ($g_{\text{op}} = 1$ for para- and $g_{\text{op}} = 2$ for ortho-transitions), $Q(T_{\text{rot}})$ is the partition function (under the high-temperature assumption), and E_l is the lower state energy of the (J, K) transition (in K).

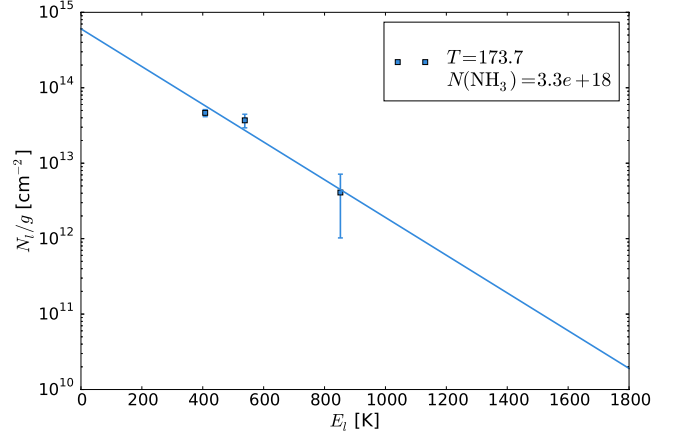


Fig. A.1. Rotational NH₃ temperatures determined for the core around the HC III region W51e2-W. The temperatures are fit to the slope of the normalized NH₃ column density N_l (in units of cm⁻³) plotted against the energy of each transition E_l (in units of Kelvins), using Eq. (A.6). Only transitions with measured optical depths were used in the fits: (6, 6), (7, 7), and (9, 9).

Since we observed more than two transitions, we can use RTDs to fit the rotational temperature and the column density simultaneously. Rearranging Eq. (A.5), using Eq. (A.4) for the column density $N(J, K)$, and taking the natural logarithm of both sides, we have

$$\begin{aligned} \log \left[7.3 \times 10^{13} \frac{J(J+1)}{K^2} \frac{1}{g_{\text{op}}(2J+1)} \frac{\Delta\nu}{\nu} \tau \right] = \\ \log \frac{N_{\text{tot}}}{T_{\text{ex}} Q(T_{\text{rot}})} - \frac{E_l}{T_{\text{rot}}}. \end{aligned} \quad (\text{A.6})$$

Equation (A.6) shows that the logarithm of the left member is a linear function of E_l (if all transitions have the same T_{ex}), with slope $-1/T_{\text{rot}}$ and intercept $\log \frac{N_{\text{tot}}}{T_{\text{ex}} Q(T_{\text{rot}})}$ at $E_l = 0$. We can then determine T_{rot} and N_{tot} from a least squares fit of lower state energy to the optical depth for different transitions in log space (Fig. A.1). In this calculation, we assume the NH₃ gas to be in LTE, and therefore $T_{\text{ex}} = T_{\text{rot}}$.

A.2. Emission

As in the case for absorption, we follow the approach for determining column density in a given rotational state from [Mangum & Shirley \(2015\)](#). For each transition, we compute N_u using the optically thin version of Eq. (30) in [Mangum & Shirley \(2015\)](#),

$$N_u = \frac{3k_B}{8\pi^3\nu\mu_{lu}^2} S_\nu f^{-1} F_\tau, \quad (\text{A.7})$$

where f is the filling fraction and $F_\tau = \frac{\tau}{1-e^{-\tau}}$ is the optical depth correction if we have computed an optical depth or 1 otherwise¹³. Line strengths μ_{lu} were retrieved from the JPL molecular database ([Pickett et al. 1998](#)) via the `astroquery`¹⁴ interface to the `splatalogue` (splatalogue.net) website. We then fit a linear function

$$\log [N(J, K)] = -E_l/T_{\text{rot}} + \log [N_{\text{tot}}/Q(T_{\text{rot}})] \quad (\text{A.8})$$

¹³ Please refer to Sect. 11 in [Mangum & Shirley \(2015\)](#) for more details on the optically thin approximation.

¹⁴ <http://www.astroquery.org/astroquery/>

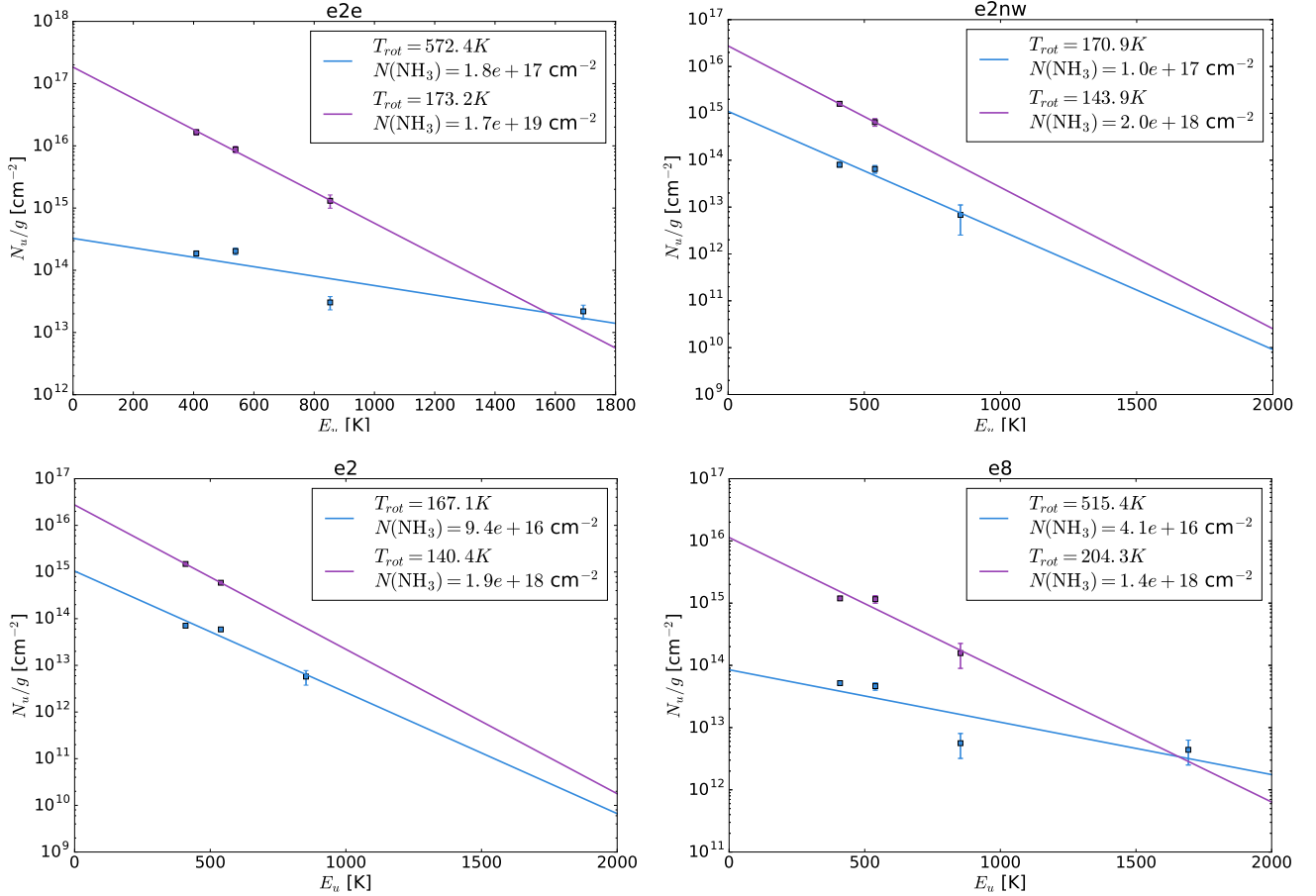


Fig. A.2. Rotational NH₃ temperatures determined for the protostars W51e2-E and W51e2-NW, and cores W51e2 and W51e8 (from left to right, and from top to bottom). The temperatures are fit to the slope of the normalized NH₃ column density N_u (in units of cm⁻³) plotted against the energy of each transition E_u (in units of Kelvins) using Eq. (A.8). The blue line is a fit to the measured columns without opacity correction. The magenta line is the fit after applying the opacity corrections, using the optical depth values in Table 3. We excluded the (10, 10) transition from the fit because of much higher rms.

to the data, where E_u is the upper energy level of a given state, N_{tot} is the total column density, and $Q(T_{\text{rot}})$ is the partition function derived using Eq. (15.48) of Wilson et al. (2009; under the high-temperature assumption).

The results of the fit are shown in Fig. A.2 for all the cores seen in NH₃ emission in W51 main.

A.3. Hyperfine line model fitting

Owing to high optical depths, simple Gaussian fitting could not accurately reproduce the observed HFS spectral profiles of the NH₃ (6, 6) and (7, 7) inversion lines both in absorption and emission. In particular, at an optical depth much larger than 10, the main hyperfine component of the NH₃ (6, 6) and (7, 7) inversion lines should be flat-topped. In contrast, the observed lines shown in Figs. 11 and 12 exhibit a Gaussian-like profile. One explanation is that the gas in the dense core is clumpy and highly structured. If a dense core is filled with pockets of hot and dense gas with a large optical depth and a small filling factor, the NH₃ spectra from these individual pockets are optically thick, hence, exhibit strong satellite hyperfines. If these pockets move at different velocities (due to infall, rotation, or turbulence), the sum of the spectra within the telescope beam can appear Gaussian-like depending on the kinematics and relative intensities of the individual spectra. The idea of a clumpy medium in relation to NH₃ spectra was discussed in the work by Sollins & Ho (2005) when analyzing high-resolution NH₃ (3, 3)

absorption spectra in G10.6-0.4. However, a detailed and exact modeling of the NH₃ spectra in W51 is beyond the scope of this paper. For a physically-motivated model explaining ammonia emission in a spatially-resolved hot-core, see, for example, Osorio et al. (2009).

Here we use a two-stage process to account for the optical depth effect when evaluating the line parameters in absorption¹⁵.

1. Because our earlier Gaussian component fitting revealed that the line profiles and centroids of the hyperfines are not always the same or even consistent with the central component, we used a model that allowed the offset of the hyperfine component to vary symmetrically around the central velocity. We assumed all components had the same intrinsic width. The central line was *not* modeled, so that the velocities and widths only come from the optically thin hyperfine lines. This fitting revealed that the hyperfine velocity offsets are only slightly different from the theoretical values given in Table 3; there were apparent differences based on the Gaussian fits, but these likely resulted from a shift in the main line's centroid. The resulting fit, along with the observed spectrum for the (6, 6) doublet, is shown in Fig. A.3.

¹⁵ This issue affects the lines both in absorption and emission, but we applied this model only to the absorption lines, which have sufficiently high S/N and narrow widths in the HF components to enable us to fit their centroids precisely.

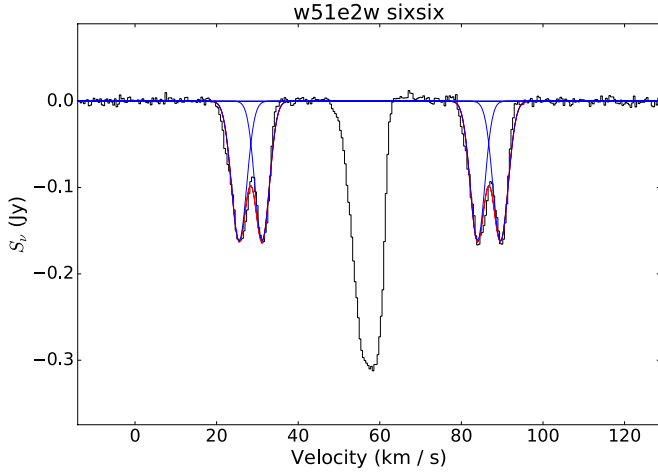


Fig. A.3. Spectrum of W51e2w in the NH₃ (6, 6) transition fitted as described in Appendix A.3.

- We modeled the hyperfines and main line simultaneously accounting for the optical depth, but keeping the offsets and widths fixed. This fit was not very good, as the hyperfines and main line cannot be explained by the same optical depth and excitation temperature. In particular, the hyperfine and main lines cannot be simultaneously modeled with an excitation temperature $T_{\text{ex}} = 2.73$ K (i.e., the coldest excitation temperature expected to be observed in a line), which is assumed in the simple approach used in point 1. In fact, both the (6, 6) and (7, 7) line profiles can be approximately reproduced if the excitation temperature $T_{\text{ex}} \sim 1800$ K and the optical depths are somewhat higher. The shape in the main line profiles is likely due to excitation temperature and optical depth variations with velocity, suggesting that there is significant unresolved velocity structure within the absorption profile (i.e., a clumpy medium).

Appendix B: NH₃ inversion lines hyperfine structure

Each NH₃ inversion transition displays a complex spectral profile due to hyperfine interactions. In particular, the interaction of the electric quadrupole moment of the nitrogen nucleus¹⁶ with the electric field due to the electrons splits each (J, K) inversion energy level into three levels characterized by the quantized nuclear spin of the nitrogen, $I_N = 1$, and the total angular momentum, $F = I_N + J$. The following selection rules apply:

$$F = (J - 1, J, J + 1), \quad \Delta F = (0, \pm 1)$$

(and obviously $\Delta K = 0$, $\Delta J = 0$ for metastable inversion lines). Therefore, each NH₃ inversion line is split into five

components: a central “main” line ($\Delta F = 0$) and two pairs of satellite lines ($\Delta F = \pm 1$), symmetrically spaced with respect to the main line¹⁷. The frequency separations of the four satellite components with respect to the main line can be calculated from the nuclear quadrupole energy, E_Q , for a symmetric molecular rotor (e.g., Townes & Schawlow 1975, Ho 1972)

$$E_Q = \frac{eqQ \left(\frac{3K^2}{J(J+1)} - 1 \right) \times [0.75C(C+1) - I_N(I_N+1)J(J+1)]}{2I_N(2I_N-1)(2J-1)(2J+3)} \quad (\text{B.1})$$

where

$$C = F(F+1) - I_N(I_N+1) - J(J+1).$$

The product $eqQ = 4.09$ is the quadrupole coupling constant, where Q is the nuclear quadrupole moment, q is the second derivative of the coulomb potential, and e is the electronic charge. The frequency separation of the outer satellites from the main line is given by $E_Q(F = J - 1) - E_Q(F = J)$, while the inner satellites are separated from the main line by $E_Q(F = J + 1) - E_Q(F = J)$. These frequency separations of the satellites are on the order of 2 MHz for the lines observed in this study and are reported in Cols. 2 and 3 of Table 3.

The intensities of the hyperfine components are given by (e.g., Townes & Schawlow 1975, P. Ho, Ph.D. Thesis, 1972)

$$I_{\text{Main}} = \frac{A [J(J+1) + F(F+1) - I_N(I_N+1)]^2 (2F+1)}{F(F+1)} \quad (\text{B.2})$$

$$(\Delta F = 0, F = J - 1, J, J + 1)$$

$$I_{\text{Sat}_1} = \frac{-A(J+F+I_N+2)(J+F-I_N+1)(J-F+I_N)(J-F-I_N-1)}{F+1}$$

$$(\Delta F = +1, F = J - 1, J)$$

$$I_{\text{Sat}_2} = \frac{-A(J+F+I_N+1)(J+F-I_N)(J-F+I_N+1)(J-F-I_N)}{F}$$

$$(\Delta F = -1, F = J, J + 1)$$

for the main line, and the two pairs of (inner and outer) satellite components, respectively¹⁸. The normalization factor A is chosen so that the total intensity across all hyperfine components is equal to 1 as follows:

$$A^{-1} = [I_{\text{Main}}(F = J - 1) + I_{\text{Main}}(F = J) + I_{\text{Main}}(F = J + 1)]$$

$$+ [I_{\text{Sat}_1}(F = J - 1) + I_{\text{Sat}_1}(F = J)]$$

$$+ [I_{\text{Sat}_2}(F = J) + I_{\text{Sat}_2}(F = J + 1)], \quad (\text{B.3})$$

(e.g., $A = 1.53 \times 10^{-4}$ for $(J, K) = (6, 6)$).

The satellites have approximately equal intensities in each pair, typically below 1% of the main line (see Col. 6 of Table 3).

¹⁶ The quadrupole moment results from the nonspherical distributions of charge within the nitrogen nucleus.

¹⁷ Weaker magnetic interactions due to spin-spin interactions among the hydrogen nuclei and the nitrogen nucleus lead to further splitting, which produces more HF components separated by up to a few tens of KHz. This is much smaller than our velocity resolution, therefore, we neglect the splitting due to magnetic interactions.

¹⁸ Note that the main line is a combination of three components, corresponding to $F = (J - 1, J, J + 1)$, which along with the two pairs of satellites, lead effectively to seven components in the HFS of NH₃ inversion lines.